High angle-of-attack aerodynamics of a straight wing with finite span using a discrete vortex method

T. M. Faure[1, a)] and C. Leogrande[1]
Centre de Recherche de l'École de l'Air, École de l'Air, 13661 Salon-de-Provence, France

(Dated: 3 October 2020)

The Leading-edge-suction-parameter modulated Discrete Vortex Method is extended to a wing with finite span and no sweep, in order to get the development of aerodynamic coefficients with angle-of-attack, from attached to completely detached flow conditions. A first case considering the unsteady pitching motion of a flat plate is compared with published experimental and numerical results. Then, dependence of lift, drag and pitching moment coefficients with angle-of-attack is discussed for a wing built on a SD7003 airfoil at constant angle-of-attack. The three-dimensional effects on the lift coefficient curve for a completely detached wing are established.

I. INTRODUCTION

In recent years, unsteady aerodynamics of wings in incompressible flow, operated on moderate Reynolds numbers in the range 10^4 to 10^5, has gained in importance, for unmanned air vehicles (UAV) and micro air vehicles (MAV) applications[1,2]. This physics is also fundamental for understanding the flapping wing motion of birds and insects. In all these applications, it is necessary to fly at conditions close to the stall point, and post-stall flight would occur during maneuvers. The present investigation focuses on the development of a low-order discrete vortex method to predict the aerodynamic performances of a finite-span wing.

The first analytical method for the estimate of lift coefficient of a constant angle-of-attack, attached flow airfoil, was the thin airfoil theory[3–5]. The unsteady solution for the lift of an airfoil undergoing a step change in angle-of-attack was solved[6]. A potential flow solution for a flat plate oscillating in pitch and plunge with a small-amplitude harmonic motion was developed[7]. Unsteady aerodynamic theories and their applications to flapping or aeroelasticity of an airfoil have been established[8,9]. These methods are valuable but are based on the potential theory, and their use is limited to fully attached flows. The adaptation of the potential theory to detached flows emerges in the 1970s with the advances in computer science, with relative limited power at that time. Vortex shedding was introduced to model the flow behind a detached body[10–12]. The detached flow behind a flat plate was numerically studied using a vortex method and a conformal transform[13,14]. The knowledge of the separation position on an airfoil allowed to adapt a discrete vortex method for a partially detached airfoil[15]. The development of more powerful computers led flow simulation toward another way with the high-order resolution of Navier-Stokes equations and closure models, and approaches like Discrete Eddy Simulation (DES), Large Eddy Simulation (LES) or Direct Numerical Simulation (DNS). However, these approaches present heavy computing costs and require long simulation time. For this reason, discrete vortex methods came back in use recently as alternative low-order methods to classical high-order Computational Fluid Dynamics (CFD), to address engineering issues with relevant accuracy. A method has been developed[16] for the prediction of continuous vortex shedding around a general sharp-edged solid body, moving in an inviscid fluid at Reynolds numbers between 100 and 1000. Discrete vortex methods have also gain in interest recently[17–20] to model flow separation downstream of a cylinder[21] or leading edge vortices[22] in unsteady flows. However, these methods are limited to start and stop criteria for the vortex shedding. This issue was addressed with the implementation of a leading edge suction parameter[23,24]. That criterion allows a wide range of applications for any airfoil geometry, with sharp or rounded leading edges, and any arbitrary motion. It proves its robustness and its relative accuracy as long as a leading edge boundary layer separation occurs and is fully validated at Reynolds numbers of 3×10^4 and 10^5. The Leading-edge-suction-parameter modulated Discrete Vortex Method (LDVM) algorithm is based, for each time step, on iterative schemes to obtain the amplitude of the last generated vortices through a converging time consuming process. A modified algorithm has been implemented[25], where the Newton-Raphson iteration search is replaced by a linear system, providing a reduction of the simulation time by a factor of 2. The method was adapted for the interaction between two airfoils with wakes and vortex shedding effects[26]. The leading-edge singularity in unsteady thin-aerofoil theory has been recently resolved[27]. However, all these discrete vortex methods are limited to airfoils and two-dimensional (2D) flows.

In the present paper, three-dimensional (3D) effects are considered coupling the LDVM with the lifting line theory[28] for a finite aspect ratio unswept wing[29]. The unsteady case of a flat plate pitching motion is first considered and compared with results of experiments and numerical simulations[30]. The dependence of lift, drag and pitching moment coefficients with angle-of-attack is provided for the unsteady flow around a fixed wing built on a SD7003 airfoil. Comparisons with available data are presented for different aspect ratios and Reynolds numbers, from low to large values of the angle-of-attack. An invariant region of the lift coefficient for angles-of-attack larger than 30° is found and the 3D effects on this curve are established.

a)Electronic mail: thierry.faure@ecole-air.fr.

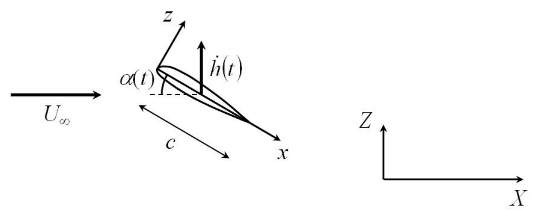

FIG. 1: Unsteady airfoil frame of reference (x,z) and aerodynamic frame of reference (X,Z).

II. 3D LDVM

A. LDVM

The founding principles and calculation parameters of the LDVM are similar to the ones presented in Ramesh et al.[23,24] and reminded in this section. The method is valid for the unsteady flow on a thin airfoil undergoing arbitrary motion. The flow can be attached or detached, but for the latter case, a leading edge separation is necessary. Some discrepancies between the actual flow and LDVM are observed if a boundary layer separation over a portion of the airfoil exists. An airfoil of chord c is placed in an upstream flow of magnitude U_∞ with an angle-of-attack $\alpha(t)$, the aerodynamic frame of reference is (X,Z) with X the direction of U_∞ and Z perpendicular to X (figure 1). The flow velocity components in this frame are U and W. The airfoil frame of reference is (x,z) with x the chordwise direction and z perpendicular to x, the velocity component normal to the airfoil is w. A plunging motion $h(t)$ of the airfoil along axis Z is modeled, but is not considered in the unsteady motion used in section III.

The time-dependent vorticity distribution along x is written as a Fourier series[5]:

$$\gamma(\theta,t) = 2U_\infty \left[A_0(t) \frac{1+\cos\theta}{\sin\theta} + \sum_{n=1}^{\infty} A_n(t) \sin n\theta \right] \quad (1)$$

with the new variable θ resulting from the transformation of the chordwise coordinate x such as:

$$x = \frac{c}{2}(1-\cos\theta)$$

The time-dependent Fourier coefficients are obtained from the velocity field $w(t)$ by enforcing the boundary condition that the flow must remain tangential to the airfoil:

$$A_0(t) = -\frac{1}{\pi}\int_0^{\pi} \frac{w(\theta,t)}{U_\infty} d\theta \quad (2)$$

$$A_n(t) = \frac{2}{\pi}\int_0^{\pi} \frac{w(\theta,t)}{U_\infty} \cos n\theta d\theta \quad (3)$$

The induced velocity normal to the airfoil is calculated from motion kinematics[31]:

$$\begin{aligned} w(x,t) = {} & \frac{\partial\eta}{\partial x}(x,t)\left[\frac{\partial\Phi_{TEV}}{\partial x}(x,t) + \frac{\partial\Phi_{LEV}}{\partial x}(x,t) \right. \\ & \left. + U_\infty\cos\alpha(t) + \dot{h}\sin\alpha(t)\right] \\ & - \frac{\partial\Phi_{TEV}}{\partial z}(x,t) - \frac{\partial\Phi_{LEV}}{\partial z}(x,t) \\ & - U_\infty\sin\alpha(t) - \dot{\alpha}(t)(x-x_p) + \dot{h}\cos\alpha(t) \end{aligned} \quad (4)$$

where Φ_{LEV} and Φ_{TEV} are the velocity potentials associated with leading edge and trailing edge vortices, η the airfoil camberline, x_p the pivot location, $\dot{\alpha}$ the time derivative of the angle-of-attack corresponding to a pitch motion and $\dot{h}$ the airfoil velocity along Z, corresponding to a plunge.

The leading-edge-suction-parameter (LESP) is a non-dimensional measure of the suction at the leading edge[8] which is equal to the first Fourier coefficient of the vorticity distribution[24]:

$$\mathrm{LESP}(t) = A_0(t)$$

The critical value LESP_{crit} corresponds to the A_0 value associated with the angle-of-attack for which spikes appear in the negative part of the friction coefficient near the leading edge suction side[24]. It is a measure of the maximum suction that a given airfoil can bear before separation and is independent of its motion[32],[33]. Parametric studies with experiments and CFD show that there is a motion independent critical value of the LESP, for a given airfoil and Reynolds number, at which leading edge vortex formation is initiated[34]. Beyond that value LESP_{crit}, the airfoil suction side boundary layer separates from the leading edge, which corresponds to the release of a leading edge vortex.

At each time step i, a trailing edge vortex (TEV) is shed. A leading edge vortex (LEV) is shed only if the LESP exceeds its critical value. The circulations associated with these LEV and TEV are obtained from Kelvin's condition:

$$\Gamma_B + \sum_{k=1}^{i}\Gamma_{TEV,k} + \sum_{l=1}^{i}\Gamma_{LEV,l} = 0 \quad (5)$$

where Γ_B is the bound circulation calculated by integrating the chordwise distribution of vorticity over the airfoil:

$$\Gamma_B = U_\infty c\pi\left[A_0(t) + \frac{A_1(t)}{2}\right] \quad (6)$$

If the LESP becomes lower than its critical value, LEV shedding is stopped. Then, the LESP concept is a single empirical parameter governing the wall viscous effect and boundary layer detachment.

Non-dimensional variables are introduced:

$$\begin{array}{ccc} w^* = \dfrac{w}{U_\infty} & U^* = \dfrac{U}{U_\infty} & W^* = \dfrac{W}{U_\infty} \\ X^* = \dfrac{X}{c} & Z^* = \dfrac{Z}{c} & \Gamma^* = \dfrac{\Gamma}{U_\infty c} \\ \eta^* = \dfrac{\eta}{c} & \dot{h}^* = \dfrac{\dot{h}}{U_\infty} & \dot{\alpha}^* = \dfrac{c}{U_\infty}\dfrac{d\alpha}{dt} \end{array}$$

The velocity induced by the kth vortex is described with the model of Vatistas et al.[35] which considers a finite core radius r_c with a solid-body rotation:

$$U_k^* = \frac{\Gamma_k^*}{2\pi} \frac{Z^* - Z_k^*}{\sqrt{\left[\left(X^* - X_k^*\right)^2 + \left(Z^* - Z_k^*\right)^2\right]^2 + r_c^{*4}}} \quad (7)$$

$$W_k^* = -\frac{\Gamma_k^*}{2\pi} \frac{X^* - X_k^*}{\sqrt{\left[\left(X^* - X_k^*\right)^2 + \left(Z^* - Z_k^*\right)^2\right]^2 + r_c^{*4}}} \quad (8)$$

with:

$$r_c^* = \frac{r_c}{c}$$

The non-dimensional time step is[24]:

$$\delta t^* = \frac{\delta t U_\infty}{c} = 0.015$$

The vortex core radius is taken to be 1.3 times the average spacing between vortices[36]:

$$r_c^* = \frac{r_c}{c} = 1.3\delta t^* = 0.02$$

The location of the new kth vortex is approximated by drawing a vector from the shedding edge to the previous shed vortex and taking the position at one-third of this distance[17], for instance for the TEV:

$$X_{TEV,k}^* = X_{TE}^* + \frac{1}{3}\left(X_{TEV,k-1}^* - X_{TE}^*\right)$$
$$Z_{TEV,k}^* = Z_{TE}^* + \frac{1}{3}\left(Z_{TEV,k-1}^* - Z_{TE}^*\right)$$

The advantage of the current approach is that account is taken not only of the wing motion since the last time step but also of the advection of the previous shed vortex, giving overall a more accurate depiction of the flow.

First, consider the case with no LEV shedding ($|\mathrm{LESP}| \leq |\mathrm{LESP}_{crit}|$). The airfoil bound circulation is equal to[25]:

$$\Gamma_B^* = I_1 + \Gamma_{TEV,i}^* I_2 \quad (9)$$

with I_1 and I_2 parameters independent from circulations computed for time step i. From Kelvin's theorem (5), we get:

$$\Gamma_{TEV,i}^* = -\frac{I_1 + \sum_{k=1}^{i-1}\Gamma_{TEV,k}^* + \sum_{l=1}^{i-1}\Gamma_{LEV,l}^*}{1 + I_2} \quad (10)$$

For the case where a LEV and a TEV are shed ($|\mathrm{LESP}| > |\mathrm{LESP}_{crit}|$), Kelvin's theorem and the condition on the critical LESP lead to[25]:

$$\Gamma_B^* + \Gamma_{TEV,i}^* + \Gamma_{LEV,i}^* + \sum_{l=1}^{i-1}\Gamma_{TEV,l}^* + \sum_{l=1}^{i-1}\Gamma_{LEV,l}^* = 0 \quad (11)$$
$$A_0 - \mathrm{LESP}_{crit} = 0 \quad (12)$$

which can be written as a linear system depending only on the unknown vortex circulations for time step i:

$$I_1 + \Gamma_{TEV,i}^*(1 + I_2) + \Gamma_{LEV,i}^*(1 + I_3) + \sum_{k=1}^{i-1}\Gamma_{TEV,l}^* + \sum_{l=1}^{i-1}\Gamma_{LEV,l}^* = 0 \quad (13)$$
$$J_1 + \Gamma_{TEV,i}^* J_2 + \Gamma_{LEV,i}^* J_3 - \mathrm{LESP}_{crit} = 0 \quad (14)$$

with I_1, I_2, I_3, J_1, J_2 and J_3 parameters independent from circulations. In addition, a condition to avoid the traversing of the camberline by a vortex has been added to the initial LDVM. This change is marginal since very few vortices are following this path. Note that for vortex circulation computation, there is no Newton-Raphson iterative loop at each time step anymore[25].

A main disadvantage of discrete vortex methods is the exponential increase in computational time with the number of vortices in the flow field. An amalgamation method based on a k-d tree of neighboring vortices[37] is adopted for vortical centers situated 4 chords downstream of the wing, in order to reduce the computing cost. Then, the simulation time is brought down from a dependence as the square of the number of shed vortices to a linear dependence[25].

The aerodynamic normal and axial forces are obtained from the Fourier coefficients[24]:

$$F_N(t) = \rho U_\infty c\pi \left[\left(U_\infty \cos\alpha + \dot{h}\sin\alpha\right)\left(A_0 + \frac{A_1}{2}\right) + c\left(\frac{3\dot{A}_0}{4} + \frac{\dot{A}_1}{4} + \frac{\dot{A}_2}{8}\right) + \rho\int_0^c \left[\left(\frac{\partial\Phi_{TEV}}{\partial x}\right) + \left(\frac{\partial\Phi_{LEV}}{\partial x}\right)\right]\gamma(x,t)\,dx\right] \quad (15)$$

$$F_A(t) = \rho\pi c U_\infty^2 A_0^2 \quad (16)$$

The lift and drag forces are obtained by:

$$L(t) = F_N(t)\cos\alpha + F_A(t)\sin\alpha \quad (17)$$
$$D(t) = F_N(t)\sin\alpha - F_A(t)\cos\alpha \quad (18)$$

Similarly for the pitching moment coefficient from the position x_{ref} :

$$M(t) = x_{ref}F_N - \rho\pi c^2 U_\infty \left\{\left(U_\infty\cos\alpha + \dot{h}\sin\alpha\right)\left(\frac{A_0}{4} + \frac{A_1}{4} - \frac{A_2}{8}\right) + c\left(\frac{7\dot{A}_0}{16} + \frac{3\dot{A}_1}{16} + \frac{\dot{A}_2}{16} - \frac{\dot{A}_3}{64}\right) - \rho\int_0^c \left[\left(\frac{\partial\Phi_{TEV}}{\partial x}\right) + \left(\frac{\partial\Phi_{LEV}}{\partial x}\right)\right]\gamma(x,t)\,x dx\right\} \quad (19)$$

Then, the aerodynamic coefficients $C_L(t)$, $C_D(t)$ are obtained dividing the forces by the upstream flow dynamic pressure multiplied by the chord, and the moment coefficient $C_M(t)$ by dividing the quarter chord moment by the upstream flow dynamic pressure multiplied by the square of the chord.

B. Lifting line theory

A wing of span b and chord c is placed in an unsteady upstream flow of magnitude U_∞ with an angle-of-attack $\alpha(t)$, the span direction in the wing frame of reference is y. Let us define the new parameter ψ such as:

$$y = -\frac{b}{2}\cos\psi$$

The wing is modeled by a distribution of horseshoe vortices along the span, providing a circulation:

$$\Gamma(\psi,t) = 2bU_\infty \sum_{n=1}^{N} P_n(t)\sin n\psi \tag{20}$$

The variation of circulation along the span results in vortex filaments being shed down the flow in accordance with Helmholtz's theorem. The shed filament has a strength equal to the spanwise derivative of circulation distribution and results in upwash and downwash on the outboard and inboard wing sections respectively[29]:

$$\frac{d\Gamma}{d\psi}(\psi,t) = 2bU_\infty \sum_{n=1}^{N} nP_n(t)\cos n\psi \tag{21}$$

The downwash at a specific spanwise station y, corresponding to a parameter ψ, resulting from all the shed filaments is given by:

$$w_i(\psi,t) = -\frac{1}{2\pi b}\int_0^\pi \frac{\frac{d\Gamma}{d\psi}(\psi^*,t)}{\cos\psi - \cos\psi^*}d\psi^* \tag{22}$$

Replacing the circulation in this expression:

$$w_i(\psi,t) = -U_\infty \sum_{n=1}^{N} nP_n(t)\frac{\sin n\psi}{\sin\psi} \tag{23}$$

C. Coupling between LDVM and lifting line theory

Consider the coupling between the 2D LDVM and the lifting line theory. Both of these methods are based on potential flow, possibly augmented for an unsteady motion and detached conditions, by the addition of vortex lines. A potential flow is characterized by a potential function Φ solution of Laplace's equation, which is a second order linear differential equation. Therefore, the superposition principle states that it is possible to add the potential functions of different potential flows, and as a consequence their velocities since $w = \partial\Phi/\partial z$. Then, the induced velocity is decomposed into:

$$w(t) = w_{2D}(\theta,t) + w_i(\psi,t) \tag{24}$$

The time-dependent Fourier coefficients of the thin airfoil theory (Eq. 2, 3) are written as[29]:

$$A_0(t) = A_{0,2D}(t) + A_{0,3D}(t)$$

$$A_n(t) = A_{n,2D}(t)$$

with:

$$A_{0,3D}(t) = \sum_{n=1}^{N} nP_n(t)\frac{\sin n\psi}{\sin\psi} \tag{25}$$

The chordwise circulation at each strip along the wing span is:

$$\Gamma(\psi,t) = U_\infty c\pi\left[A_{0,2D}(t) + A_{0,3D}(t) + \frac{A_{1,2D}(t)}{2}\right] \tag{26}$$

It has been shown that there is no influence of the number of 2D spanwise sections on the flow solution, from 9 sections along the wing. The lift, drag and pitching moment coefficients are obtained integrating along the wing, the coefficients obtained for each section. A disadvantage of the coupling between the 2D LDVM and the lifting line theory is that it is only valid for unswept wings with planar wakes. Vortices shed for a spanwise station are assumed to have a negligible effect on vortices shed from other spanwise stations[29].

III. UNSTEADY MOTION OF A FLAT PLATE

The generation of LEV on an accelerating or pitching flat plate is a benchmark case for the validation of numerical methods, from low to medium Reynolds numbers[19,30,38,39]. The 3D LDVM is compared with published data[30] for a wing aspect ratio of 4 built on an airfoil section which is a flat plate, at Reynolds numbers between 30 and 40,000. The flat plate wing motion is a translational rectilinear pitch, meaning a pitch about a spanwise-aligned axis placed at the leading edge, in steady free-stream. The history of the angle-of-attack is a linear ramp with smoothed corners, according to the Eldredge function[40] (figure 2). Non-dimensional time $t^* = 0$ corresponds to the beginning of increase in angle-of-attack α from $0°$, and $t^* = 1$ corresponds to the end of the ramp with $\alpha = 45°$. The lift and drag coefficients presented hereafter correspond to water tunnel measurements (Stevens and Cetiner at $Re = 10,000$, Granlund, Yu and Mancini at $Re = 20,000$)

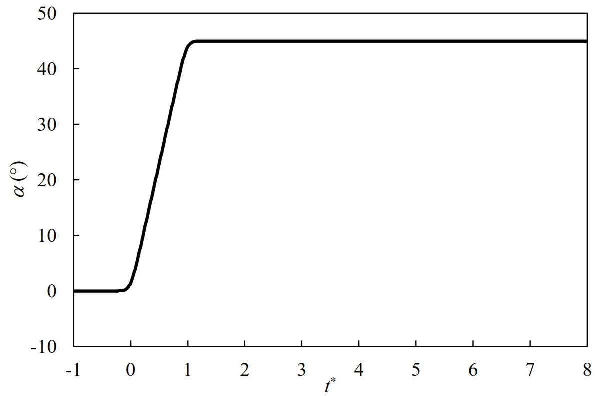

FIG. 2: History of the fast ramp in pitch using the Eldredge function[40], with a constant free-stream.

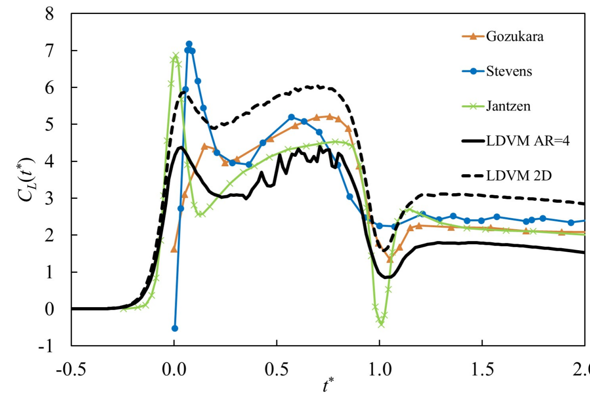

FIG. 3: Comparison of lift coefficient short time history between the 2D and 3D LDVM and data[30] for the flat plate fast pitch with $A_R = 4$.

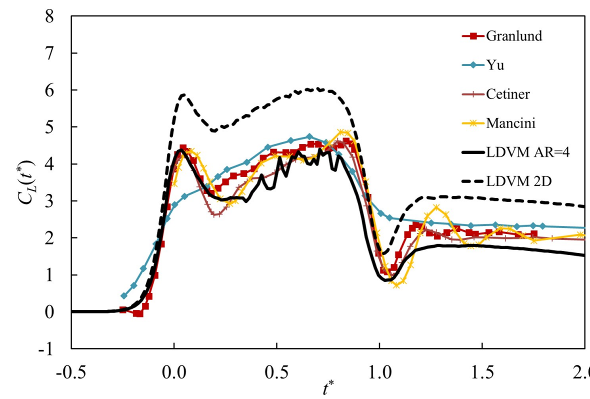

FIG. 4: Comparison of lift coefficient short time history between the 2D and 3D LDVM and data[30] for the flat plate fast pitch with $A_R = 4$ (continued).

or CFD simulations (Reynolds-averaged Navier-Stokes equations computations from Gozukara at $Re = 3600$ and $10,000$, and immersed boundary method on a Cartesian Lagrangian grid from Jantzen at $Re = 300$). It has been shown[30] that lift history is weakly dependent on Reynolds number from $Re > 100$, as soon as LEV formation occurs.

Figures 3 and 4 present the lift coefficients for the aforementioned data sets compared with the 2D LDVM[24,25] and present 3D LDVM for a wing aspect ratio $A_R = 4$. For both LDVM simulations, the Reynolds number is $10,000$. In order to avoid too many graphs on the same figure and to compare the different data sets with the 2D LDVM and 3D LDVM, the development of the lift coefficient is presented in two different figures. In figures 3 and 4, a first maximum lift coefficient is generally found around $t^* = 0$ and corresponds to a LEV generation associated with a leading edge detachment. In data of Stevens and Jantzen (figure 3), this peak is even larger than the prediction of the 2D LDVM, which predicts larger values than the 3D LDVM. However, between $t^* = 0.25$ and 1 the amplitude of $C_L(t^*)$ is lower than the 2D LDVM prediction. A second maximum is observed around $t^* = 0.7$, with an amplitude larger than the first maximum in some data sets, and placed between $t^* = 0.5$ and 0.9, followed by a drop around $t^* = 1$ and a rise. A good agreement between the various data sets is observed in figure 4, which match much more with the 3D LDVM than with the 2D LDVM. Note that the peak (around $t^* = 0$) and valley (around $t^* = 1$) associated with the rapid change in angle of attack are not present in Yu.

Figures 5 and 6 are the lift coefficient history up to $t^* = 8$. Previous data for wings and the 3D LDVM tend to converge toward a lift coefficient around 1.4 for $t^* > 3$, which is not the case for the 2D LDVM which exhibits larger values. The 3D LDVM presents periodic oscillations not observed in the other simulations or experiments, with, for $t^* > 3$, a component associated with a period $T^* \sim 3$. Since the Strouhal number is defined, for an airfoil with an angle of attack α, as:

$$St = \frac{fc\sin\alpha}{U_\infty} = \frac{\sin\alpha}{T^*} = 0.23$$

This value is close to the value around 0.2 observed downstream of an airfoil if a vortex shedding is present[41,42]. Therefore, the oscillations may be due to the periodic LEV and TEV shedding downstream of the wing, for completely detached flow at large angle-of-attack, as the ones observed for a flat plate[39]. The fact that these modulations are not observed in most of the lift coefficient data[30] is probably due to signal-to-noise filtering in the experiments.

Figures 7 and 8 are the time development of drag coefficient for the same data sets. Again, a good agreement is observed, particularly for the rise of drag coefficient associated with the increase in angle-of-attack up to a maximum for $t^* = 0.9$ and the rapid drop with a minimum for $t^* = 1.1$. Note that the time position and amplitude of the maximum are well predicted by 3D LDVM while the 2D LDVM evaluation is 40% higher. For other times, the 2D LDVM still presents much larger values than the experiments and simulations for wings with $A_R = 4$, while the 3D LDVM fits better with the data sets, evidence that the finite span of the wing is taken into account in the method. As for $C_L(t^*)$, periodic oscillations are observed in LDVM for $C_D(t^*)$, associated with the periodic shedding.

The spanwise flow visualization along the wing for $A_R = 4$ is presented in figure 10 for the positions $y/b = 0.25, 0.375$ and

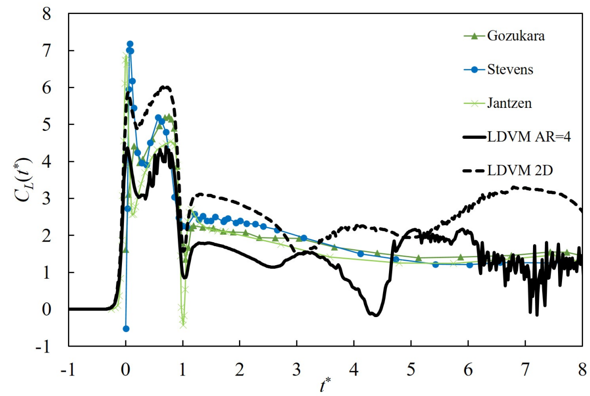

FIG. 5: Comparison of lift coefficient long time history between the 2D and 3D LDVM and data[30] for the flat plate fast pitch with $A_R = 4$.

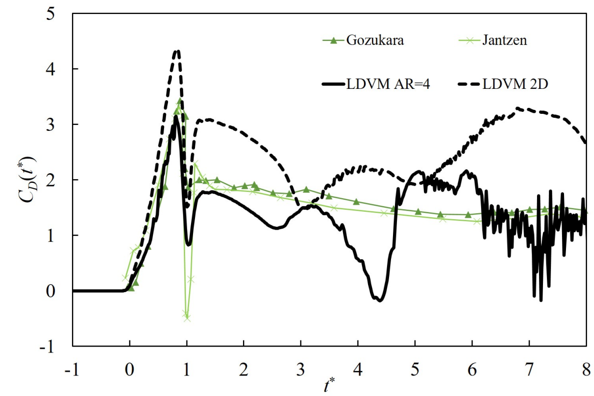

FIG. 7: Comparison of drag coefficient long time history between the 2D and 3D LDVM and data[30] for the flat plate fast pitch with $A_R = 4$.

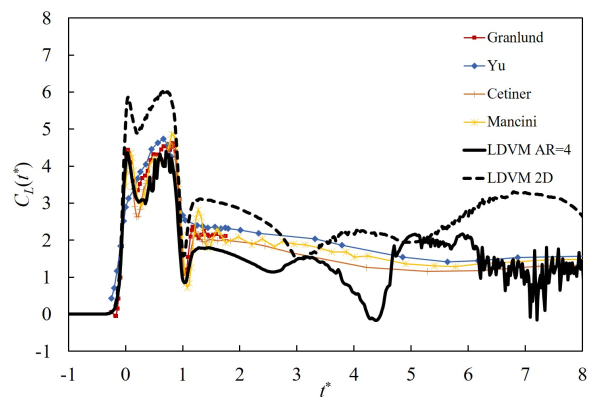

FIG. 6: Comparison of lift coefficient long time history between the 2D and 3D LDVM and data[30] for the flat plate fast pitch with $A_R = 4$ (continued).

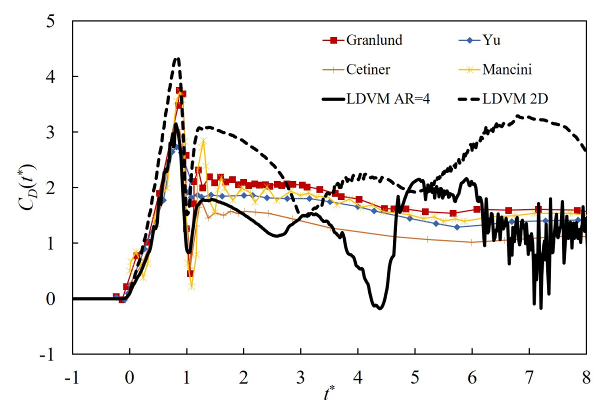

FIG. 8: Comparison of drag coefficient long time history between the 2D and 3D LDVM and data[30] for the flat plate fast pitch with $A_R = 4$ (continued).

0.5 (figure 9) and angles of attack $\alpha = 23°$, $38°$ and $45°$. The 3D LDVM represents the circulation of the computed vortex centers (circulation negative in blue, close to 0 in green and positive in red) at a Reynolds number of 10,000. These results are compared with planar laser illumination of fluorescent dye in a water tunnel[30] at a Reynolds number of 20,000. For $\alpha = 23°$ (figures 10a and 10d) a LEV develops and the starting TEV is advected downstream. There are very little discrepancies between the flow fields at $y/b = 0.25$ and 0.375 but the 3D effects are clearly identified for $y/b = 0.5$, corresponding to the influence of the wing tip vortex. For $\alpha = 38°$ (figures 10b and 10e), the LEV is larger at $y/b = 0.25$ and 0.375 and the flow is relatively similar, but the tip vortex induces a complete flow detachment for $y/b = 0.5$. For $\alpha = 45°$ (figures 10c and 10f), the LEV is completely developed at stations $y/b = 0.25$ and 0.375 and the tip vortex effects are larger. The spanwise modulations of the 3D LDVM are clearly identified from the spanwise flow development along the wing. These results are qualitatively in good agreement with the experiments.

The vortices created on and downstream of the wing of $A_R = 4$ are compared with particle image velocimetry (PIV) measurements and the 3D LDVM simulations in figure 11, for different non-dimensional times. The spanwise location is $y/b = 0.25$, circulation is plotted for the 3D LDVM (negative in blue, close to 0 in green and positive in red) while PIV fields are provided with vorticity (negative in blue and positive in red). Note a relative good agreement between the 3D LDVM and the PIV measurements. For $t^* = 0.5$ (figures 11a and 11b), the wing suction side is detached and a LEV is forming and develops up to the final angle-of-attack $\alpha = 45°$ for $t^* = 1$ (figures 11c and 11d). This first LEV is still developing and is shed downstream from the wing at $t^* = 2.5$ (figures 11g and 11h). The generation of a new TEV at $t^* = 3$, and the development of a periodic Kármán street, is more clearly observed in the 3D LDVM (figures 11i and 11j). At $t^* = 5.5$ a second LEV appears to be forming (figures 11k and 11l). The periodic generation of LEV and TEV in the 3D LDVM simulations could explain the oscillations in lift and drag coefficients observed in figures 5, 6, 7 and 8, as previously observed in LES combined with an immersed boundary method[39].

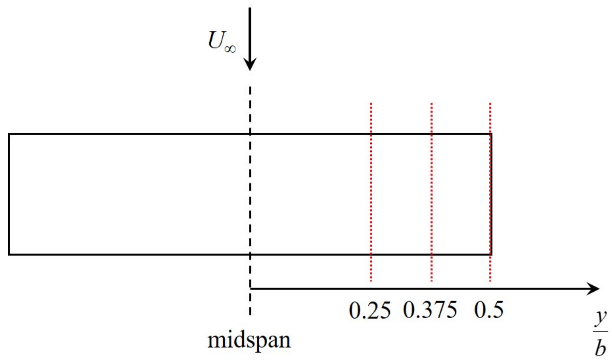

FIG. 9: Spanwise positions of flow visualization near the wing tip.

IV. WING AT CONSTANT ANGLE-OF-ATTACK

The 3D LDVM considers now the unsteady flow around a wing at constant angle-of-attack. A long simulation up to $t^* = 45$ is conducted to obtain time-averaged values of lift, drag and quarter-chord pitching moment coefficients for each value of the angle-of-attack. As different airfoil wing sections are compared, each aerodynamic coefficient is plotted versus $\alpha - \alpha_{L=0}$, with $\alpha_{L=0}$ the zero lift angle-of-attack, to get rid of the camber effect in the positioning of each curve. Figure 12 presents the lift coefficient for small values of the angle-of-attack, for which the flow is attached on the wing suction side and a small portion of the post-stall region. The 2D LDVM simulations consider a SD7003 airfoil at $Re = 2.1 \times 10^4$. The 3D LDVM simulations consider a wing with an aspect ratio of 8 built on a SD7003 airfoil at $Re = 2.1 \times 10^4$. The 2D detached eddy simulation of a NACA 23 012 at $Re = 5.8 \times 10^4$ is also plotted[43] with the measurements of a wing built on a circular arc airfoil[44] with $A_R = 4$ at $Re = 2.1 \times 10^4$. For attached flow conditions, the slope predicted by the thin airfoil theory, and its correction for wings of aspect ratios of 4 and 8 are also provided in the figure. The stall point of each wing is different, because of different camberlines, but it is observed around $\alpha - \alpha_{L=0} = 15°$. On the left of this point, each plot fits very well with the slope predicted by the thin airfoil theory corrected with aspect ratio. On the right of the stall, the drop of the lift coefficient is strongly dependent on the airfoil wing section, but two different trends can be observed. Figure 13 presents the lift coefficient up to $\alpha - \alpha_{L=0} = 90°$, with the addition of the 2D RANS simulation using a $k - \omega$ turbulence model[45] of a SD7003 airfoil at $Re = 6 \times 10^4$, measurements[46] around a wing of $A_R = 3.67$ built on a NACA $65_4 - 421$ airfoil at $Re = 4 \times 10^5$, measurements[47] around a wing of $A_R = 6$ built on a NACA 0012 airfoil at $Re = 3.6 \times 10^5$ and measurements[48] around a wing of $A_R = 4.1$ built on a NACA 0012 airfoil at $Re = 6.2 \times 10^4$. For $\alpha - \alpha_{L=0} > 30°$, the lift coefficient presents a hump-like shape, with a larger height for the 2D LDVM and a maximum around 2.4. For the wings, including the 3D LDVM for $A_R = 8$, a similar hump is observed, independent on Reynolds number and aspect ratio, but with a lower maximum around 1.2 observed for $\alpha - \alpha_{L=0} = 45°$.

Similar comments are valid for the drag coefficient presented for the very same references in figure 14. Low values of the drag coefficient are observed for $\alpha - \alpha_{L=0} < 15°$, and a rapid rise after the stall. Note that the 2D LDVM reaches a maximum around 2.7 while the drag coefficient is limited to a value around 1 for wings at $Re \sim 6 \times 10^4$ fitting relatively well with the 3D LDVM for $Re \sim 2.1 \times 10^4$. For $Re \sim 4 \times 10^5$, the drag coefficient reaches a maximum around 1.8, and a development with the angle of attack between the predictions of 2D LDVM and 3D LDVM. The discrepancy between the drag coefficient values at large angle-of-attack could be caused by the difference of one order in magnitude in the Reynolds numbers. Different surface roughness between experiments[46,47] and flow simulations[48] could also explain these discrepancies for $\alpha > 30°$. However, the main reason is probably due to the experimental set-up, the wing is placed between two panels to obtained a 2D flow[46,47], condition which is no longer completely obtained for a detached flow above 30°.

The quarter-chord pitching moment coefficient is presented in figure 15 for the 2D and 3D LDVM and measurements[46,47]. For large values of the angle-of-attack, the drop beyond $\alpha = 30°$ is larger for the 2D LDVM than for finite span wings. Note the much lower values of this coefficient in comparison with lift and drag coefficients, which can explain a larger scattering of points.

V. CONCLUSION

The LDVM is extended, considering 3D effects resulting from a finite span wing, coupling the 2D LDVM with the lifting line theory. This results in the addition of a supplementary term in the first Fourier coefficient of the circulation development[5]. The extended 3D LDVM is validated with the unsteady motion of a flat plate of aspect ratio $A_R = 4$ for a medium Reynolds number of 10,000. A good agreement is found between previous experimental and numerical results, for the time development of lift, drag and pitching moment coefficients as well as vorticity temporal snapshots. The spanwise flow modulation induced by the finite-width and the generation of the wing tip vortex is clearly considered by the 3D LDVM, the flow simulations fitting with experimental visualizations. Thus, the 3D LDVM is an appropriate low-order method for flow predictions around a wing and applications in engineering problems for a medium range of Reynolds numbers. The 3D LDVM is also used for the long duration flow simulation of the unsteady flow around a constant angle-of-attack wing. For attached flow conditions, the LDVM simulations fit very well with the thin airfoil theory and its correction with wing aspect ratio. For large values of the angle-of-attack, corresponding to a completely detached wing, a great discrepancy between the 2D LDVM and 3D LDVM predictions are founds. However, the 3D LDVM is in accordance with measurements in these regions, evidence of the effects of finite span on the aerodynamic coefficients. An invariant hump-like shaped plot of the lift coefficient versus angle-of-attack is found for $\alpha > 30°$ for a finite span wing, with a maximum around 1.15 for $\alpha = 45°$.

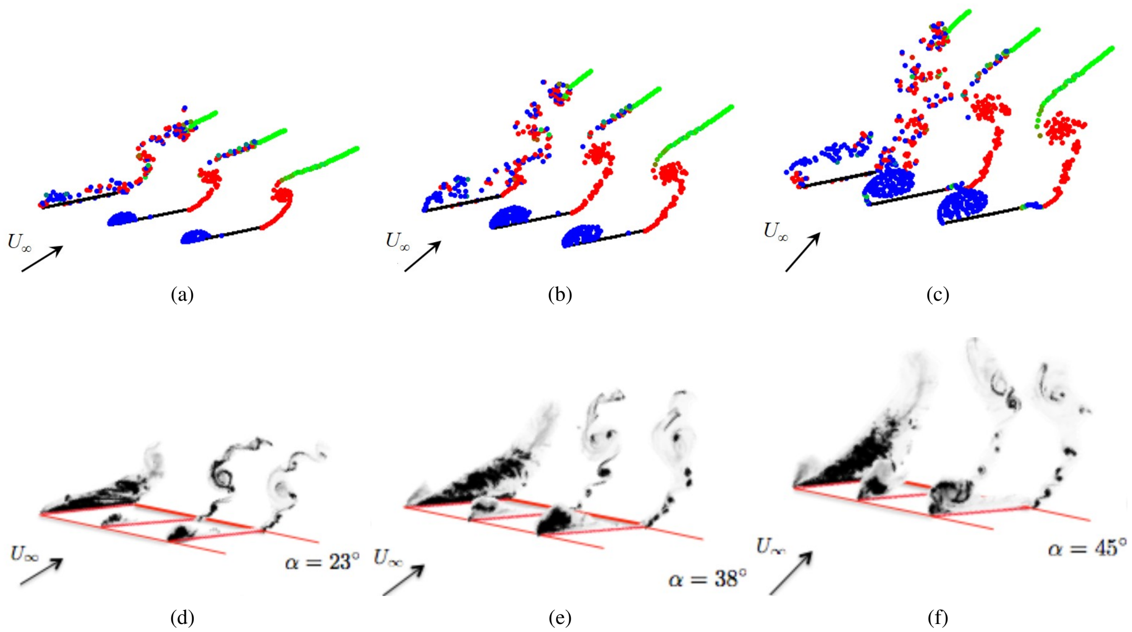

FIG. 10: Flow visualization along the wing built on a flat plate with $A_R = 4$ for three different spanwise position $y/b = 0.25$, 0.375 and 0.5: comparison between the 3D LDVM at $Re = 10,000$ (circulation negative in blue, close to 0 in green and positive in red) and planar laser illumination of fluorescent dye in a water tunnel[30] (reproduced with permission from NATO STO Technical Paper TR-AVT-202 (2016) Copyright STO/NATO 2016) at $Re = 20,000$ for (a) 3D LDVM, $t^* = 0.5$, $\alpha = 23°$, (b) 3D LDVM, $t^* = 0.75$, $\alpha = 38°$, (c) 3D LDVM, $t^* = 1$, $\alpha = 45°$, (d) flow visualization, $t^* = 0.5$, $\alpha = 23°$, (e) flow visualization, $t^* = 0.75$, $\alpha = 38°$, (f) flow visualization, $t^* = 1$, $\alpha = 45°$.

DATA AVAILABILITY STATEMENT

The data that supports the findings of this study are available within the article.

REFERENCES

[1] T. J. Mueller and J. D. DeLaurier, "Aerodynamics of small vehicles," Annual Review of Fluid Mechanics **35**, 89–111 (2003).

[2] J. Winslow, H. Otsuka, B. Govindarajan, and I. Chopra, "Basic understanding of airfoil characteristics at low Reynolds numbers (10^4–10^5)," Journal of Aircraft **55**, 1050–1061 (2018).

[3] M. Munk, "General theory of thin wing sections," Tech. Rep. (142 NACA, 1922).

[4] W. Birnbaum, "Die tragende Wirbelfläche als Hilfsmittel zur Behandlung des ebenen Problems der Tragflügeltheorie," ZAMM-Journal of Applied Mathematics and Mechanics/Zeitschrift für Angewandte Mathematik und Mechanik **3**, 290–297 (1923).

[5] H. Glauert, *The elements of aerofoil and airscrew theory* (Cambridge University Press, 1926).

[6] H. Wagner, "Über die Entstehung des dynamischen Auftriebes von Tragflügeln," Z. Angew. Math. Mech. **5**, 17–35 (1925).

[7] T. Theodorsen, "General theory of aerodynamic instability and the mechanism of flutter," Tech. Rep. (496 NACA, 1935).

[8] I. E. Garrick, "Propulsion of a flapping and oscillating airfoil," Tech. Rep. (NACA TN-D-85, 1937).

[9] T. von Kármán and W. Sears, "Aerofoil theory for non-uniform motion," Journal of Aeronautical Science **5**, 379–390 (1938).

[10] R. R. Clements, "An inviscid model of two-dimensional vortex shedding," Journal of Fluid Mechanics **57**, 321–336 (1973).

[11] R. R. Clements and D. J. Maull, "The representation of sheets of vorticity by discrete vortices," Progress in Aerospace Science **16**, 129–146 (1975).

[12] M. Kiya and M. Arie, "A contribution to an inviscid vortex-shedding model for an inclined flat plate in uniform flow," Journal of Fluid Mechanics **82**, 241–253 (1977).

[13] K. Kuwahara, "Numerical study of flow past an inclined flat plate by an inviscid model," Journal of the Physical Society of Japan **35**, 1545 (1973).

[14] T. Sarpkaya, "An inviscid model of two-dimensional vortex shedding for transient and asymptotically steady separated flow over an inclined plate," Journal of Fluid Mechanics **68**, 109–128 (1975).

[15] J. Katz, "Discrete vortex method for the the non-steady separated flow over an aerofoil," Journal of Fluid Mechanics **102**, 315–328 (1981).

[16] S. Michelin and S. G. L. Smith, "An unsteady point vortex method for coupled fluid–solid problems," Theoretical and Computational Fluid Dynamics **23**, 127–153 (2009).

[17] S. A. Ansari, R. Zbikowski, and K. Knowles, "A nonlinear unsteady aerodynamic model for insect-like flapping wings in the hover. Part 2: implementation and validation," Proceedings of the Institution of Mechanical Engineers, Part G: Journal of Aerospace Engineering **30**, 169–186 (2006).

[18] C. Wang and J. D. Eldredge, "Low-order phenomenological modelling of leading-edge vortex formation," Theoretical Computational Fluid Dynamics **27**, 577–598 (2013).

[19] X. Xia and K. Mohseni, "Lift evaluation of a two-dimensional pitching flat plate," Physics of Fluids **25**, 091901 (2013).

[20] P. Hammer, A. Altman, and F. Eastep, "Validation of a discrete vortex method for low Reynolds number unsteady flow," AIAA Journal **52**, 643–649 (2014).

[21] M. André de Oliveira, P. Guimarães de Moraes, C. Lilian de Andrade, A. Mendonça Bimbato, and L. A. Alcântara Pereira, "Control and suppression of vortex shedding from a slightly rough circular cylinder by a discrete vortex method," Energies **13**, 4481 (2020).

[22] A. Gumerov, "Simulation of separated flow past an inclined and normal plates by a discrete vortex method," IOP Conference Series: Materials Science and Engineering **890**, 012161 (2020).

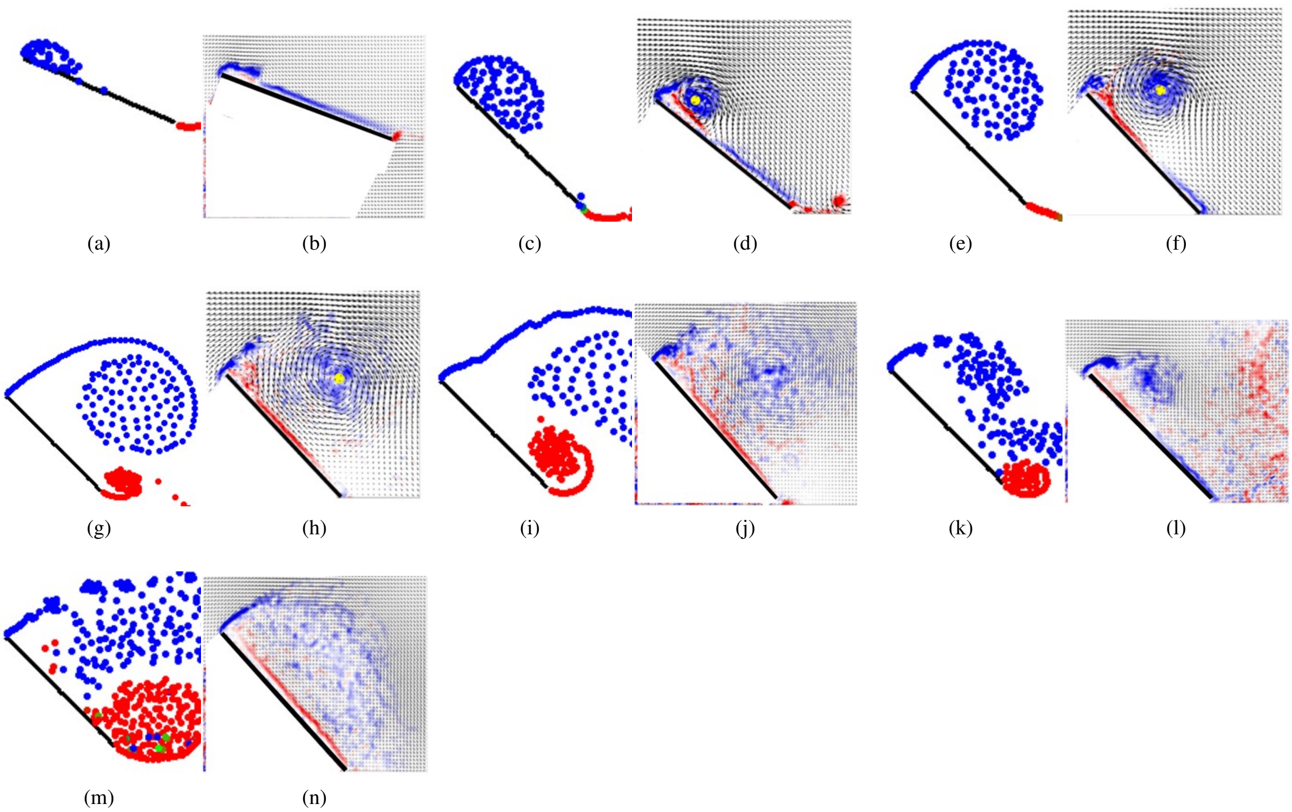

FIG. 11: Comparison between the 3D LDVM, circulation negative in blue, close to 0 in green and positive in red, and PIV measurements[30] (reproduced with permission from NATO STO Technical Paper TR-AVT-202 (2016) Copyright STO/NATO 2016), velocity field and vorticity negative in blue and positive in red, for a flate plate with $A_R = 4$ and a spanwise position $^y/_b = 0.25$ for (a) 3D LDVM, $t^* = 0.5$, (b) PIV, $t^* = 0.5$, (c) 3D LDVM, $t^* = 1$, (d) PIV, $t^* = 1$, (e) 3D LDVM, $t^* = 1.5$, (f) PIV, $t^* = 1.5$, (g) 3D LDVM, $t^* = 2.5$, (h) PIV, $t^* = 2.5$, (i) 3D LDVM, $t^* = 3$, (j) PIV, $t^* = 3$, (k) 3D LDVM, $t^* = 5.5$, (l) PIV, $t^* = 5.5$, (m) 3D LDVM, $t^* = 8$ and (n) PIV, $t^* = 8$.

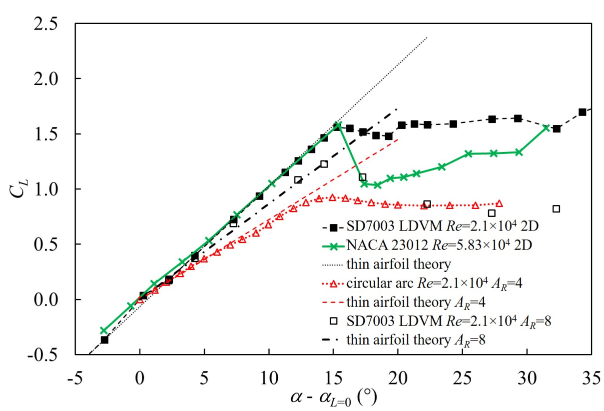

FIG. 12: Lift coefficient versus angle-of-attack up to 35° obtained from the 2D and 3D LDVM compared with other data[43,44].

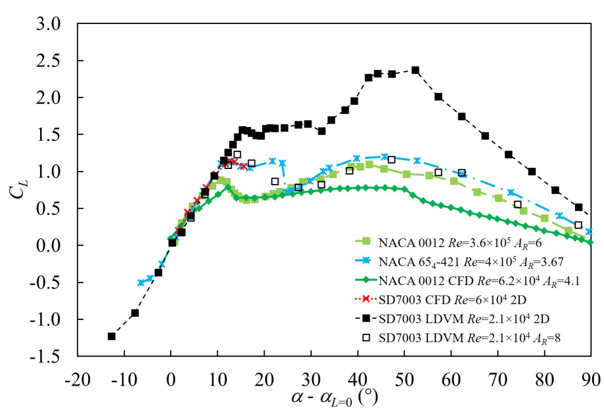

FIG. 13: Lift coefficient versus angle-of-attack obtained from the 2D and 3D LDVM compared with other data[45–48].

[23] K. Ramesh, A. Gopalarathnam, J. R. Edwards, M. V. Ol, and K. Granlund, "An unsteady airfoil theory applied to pitching motions validated against experiments and computation," Theoretical and Computational Fluid Dynamics **27**, 843–864 (2013).

[24] K. Ramesh, A. Gopalarathnam, K. Granlund, M. V. Ol, and J. R. Edwards, "Discrete-vortex method with novel shedding criterion for unsteady aerofoil flows with intermittent leading-edge vortex shedding," Journal of Fluid Mechanics **751**, 500–538 (2014).

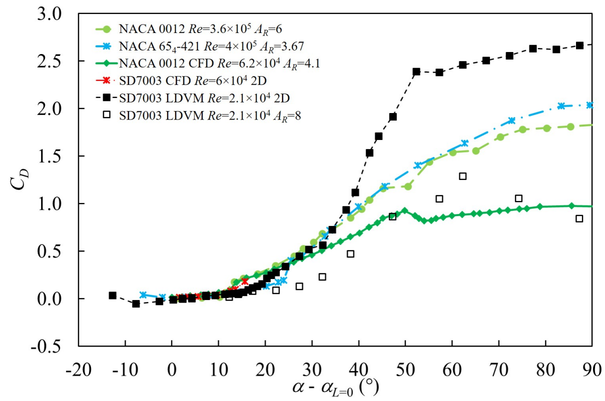

FIG. 14: Drag coefficient versus angle-of-attack obtained from the 2D and 3D LDVM compared with other data[45–48].

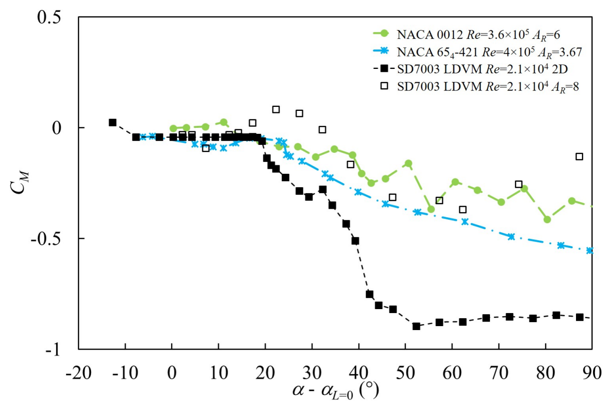

FIG. 15: Quarter-chord pitching moment coefficient versus angle-of-attack obtained from the 2D and 3D LDVM compared with other data[46,47].

[25]T. M. Faure, L. Dumas, V. Drouet, and O. Montagnier, "A modified discrete-vortex method algorithm with shedding criterion for aerodynamic coefficients prediction at high angle of attack," Applied Mathematical Modelling **69**, 32–46 (2019).

[26]T. M. Faure, L. Dumas, and O. Montagnier, "Numerical study of two-airfoil arrangements by a discrete vortex method," Theoretical and Computational Fluid Dynamics **34**, 79–103 (2020).

[27]K. Ramesh, "On the leading-edge suction and stagnation point location in unsteady flows past thin aerofoils," Journal of Fluid Mechanics **886**, A13 (2020).

[28]L. Prandtl, "Applications of modern hydrodynamics to aeronautics," Tech. Rep. 116 NACA (1923).

[29]K. Ramesh, T. P. Monteiro, F. J. Silvestre, A. B. Guimaraes Neto, T. de Souza Siqueira Versiani, and R. G. Annes da Silva, "Experimental and numerical investigation of post-flutter limit cycle oscillations on a cantilevered flat plate," in *International Forum on Aeroelasticity and Structural Dynamics, IFASD 2017* (Como, Italy, 2017) 25-28 June.

[30]M. V. Ol and H. Babinsky, "Extensions of fundamental flow physics to practical mav aerodynamics," Tech. Rep. NATO STO TR-AVT-202 (2016).

[31]J. Katz and A. Plotkin, *Low-Speed Aerodynamics* (Cambridge University Press, 2001).

[32]K. Ramesh, A. Gopalarathnam, M. V. Ol, K. Granlund, and J. R. Edwards, "Augmentation of inviscid airfoil theory to predict and model 2D unsteady vortex dominated flows," in *41st AIAA Fluid Dynamics Conference and Exhibit* (Honolulu, Hawai, USA, 2011) AIAA Paper 2011-3578.

[33]K. Ramesh, *Theory and Low-Order Modeling of Unsteady Airfoil Flows*, Ph.D. thesis, North Carolina State University, Rayleigh, NC, USA (2013).

[34]K. Ramesh, K. Granlund, M. V. Ol, A. Gopalarathnam, and J. R. Edwards, "Leading-edge flow criticality as a governing factor in leading-edge vortex initiation in unsteady airfoil flows," Theoretical and Computational Fluid Dynamics **32**, 109–136 (2018).

[35]G. H. Vatistas, V. Kozel, and W. C. Mih, "A simpler model for concentrated vortices," Experiments in Fluids **11**, 73–76 (1991).

[36]A. Leonard, "Vortex methods for flow simulation," Journal of Computational Physics **37**, 289–335 (1980).

[37]J. L. Bentley, "Multidimensional binary search trees used for associative searching," Communications of the ACM **18**, 509–517 (1975).

[38]K. K. Chen, T. Colonius, and K. Taira, "The leading-edge vortex and quasisteady vortex shedding on an accelerating plate," Physics of Fluids **22**, 033601 (2010).

[39]X. Zhang and J. Schlüter, "Numerical study of the influence of the Reynolds-number on the lift created by a leading edge vortex," Physics of Fluids **24**, 065102 (2012).

[40]J. D. Eldredge, C. J. Wang, and M. V. Ol, "A computational study of a canonical pitch-up, pitch down wing maneuver," (2009) AIAA Paper 2009-3687.

[41]C. Sicot, S. Aubrun, S. Loyer, and P. Devinant, "Unsteady characteristics of the static stall of an airfoil subjected to freestream turbulence level up to 16%," Experiments in Fluids **41**, 641–648 (2006).

[42]T. M. Faure, L. Hétru, and O. Montagnier, "Aerodynamic features of a two-airfoil arrangement," Experiments in Fluids **58**, 146 (2017).

[43]L. Hétru, *Étude expérimentale et numérique de l'interaction aérodynamique entre deux profils : application au risque aéronautique du décrochage profond*, Ph.D. thesis, Université d'Aix-Marseille, France (2015).

[44]E. V. Laitone, "Wind tunnel tests of wings at Reynolds numbers below 70 000," Experiments in Fluids **23**, 405–409 (1997).

[45]Y. Lian and W. Shyy, "Laminar-turbulent transition of a low reynolds number rigid or flexible airfoil," AIAA journal **45**, 1501–1513 (2007).

[46]P. Devinant, T. Laverne, and J. Hureau, "Experimental study of wind-turbine airfoil aerodynamics in high turbulence," Journal of Wind Engineering and Industrial Aerodynamics **90**, 689–707 (2002).

[47]R. E. Sheldahl and P. C. Klimas, "Aerodynamic characteristics of seven symmetrical airfoil sections through 180-degree angle of attack for use in aerodynamic analysis of vertical axis wind turbines," Tech. Rep. (Sandia National Labs., Albuquerque, NM (USA), 1981).

[48]S. Worasinchai, G. Ingram, and R. Dominy, "A low-reynolds-number, high-angle-of-attack investigation of wind turbine aerofoils," Proceedings of the Institution of Mechanical Engineers, Part A: Journal of Power and Energy **225**, 748–763 (2011).

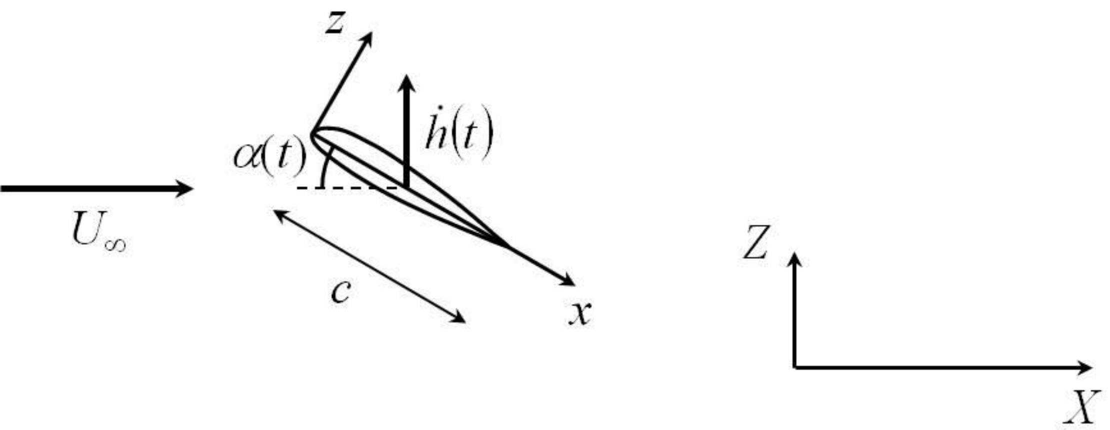

z
$\dot{h}(t)$
$\alpha(t)$
U_∞
c
x
Z
X

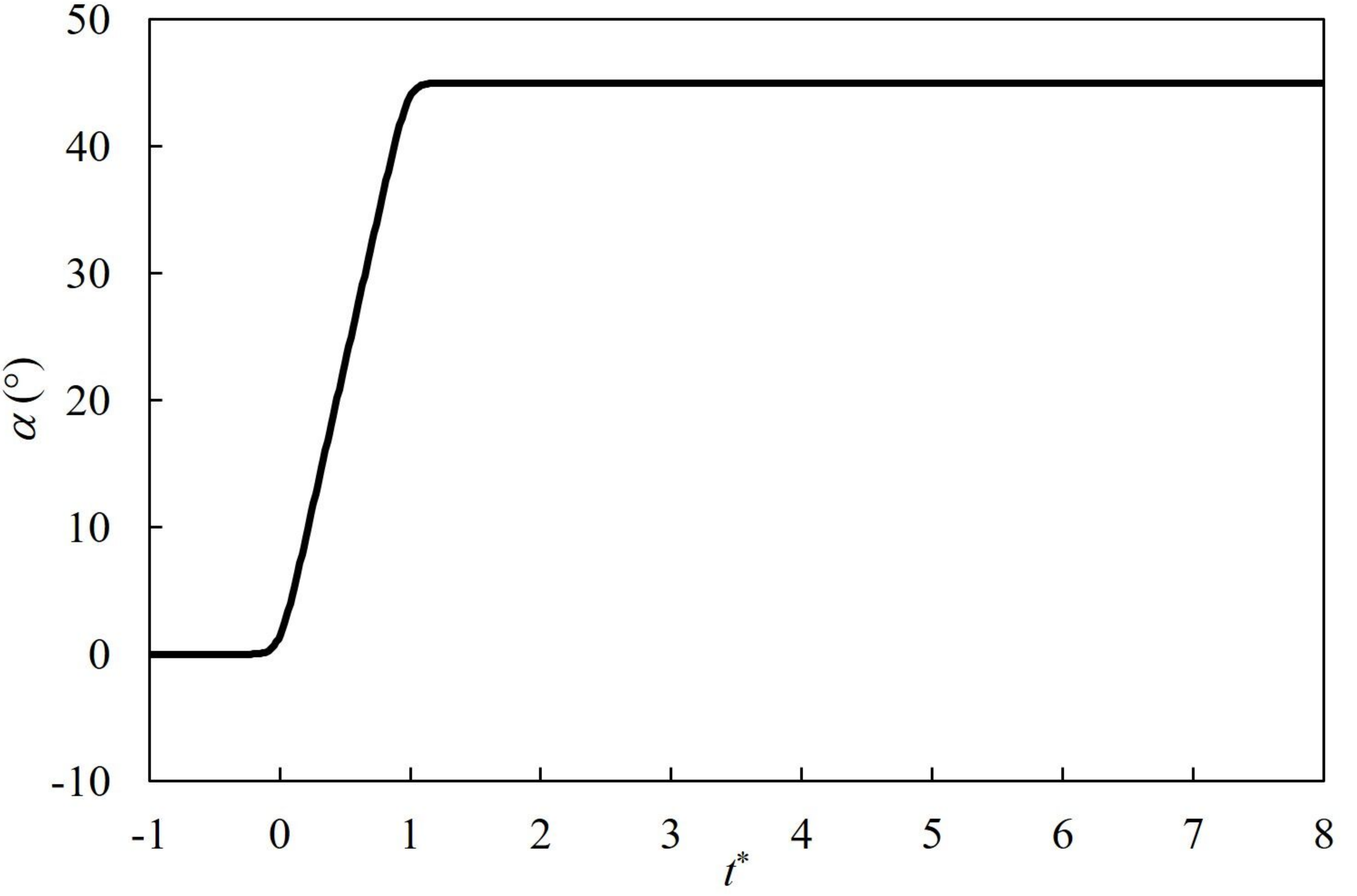

50
40
30
20
10
0
-10
α (°)
-1
0
1
2
3
4
5
6
7
8
t*

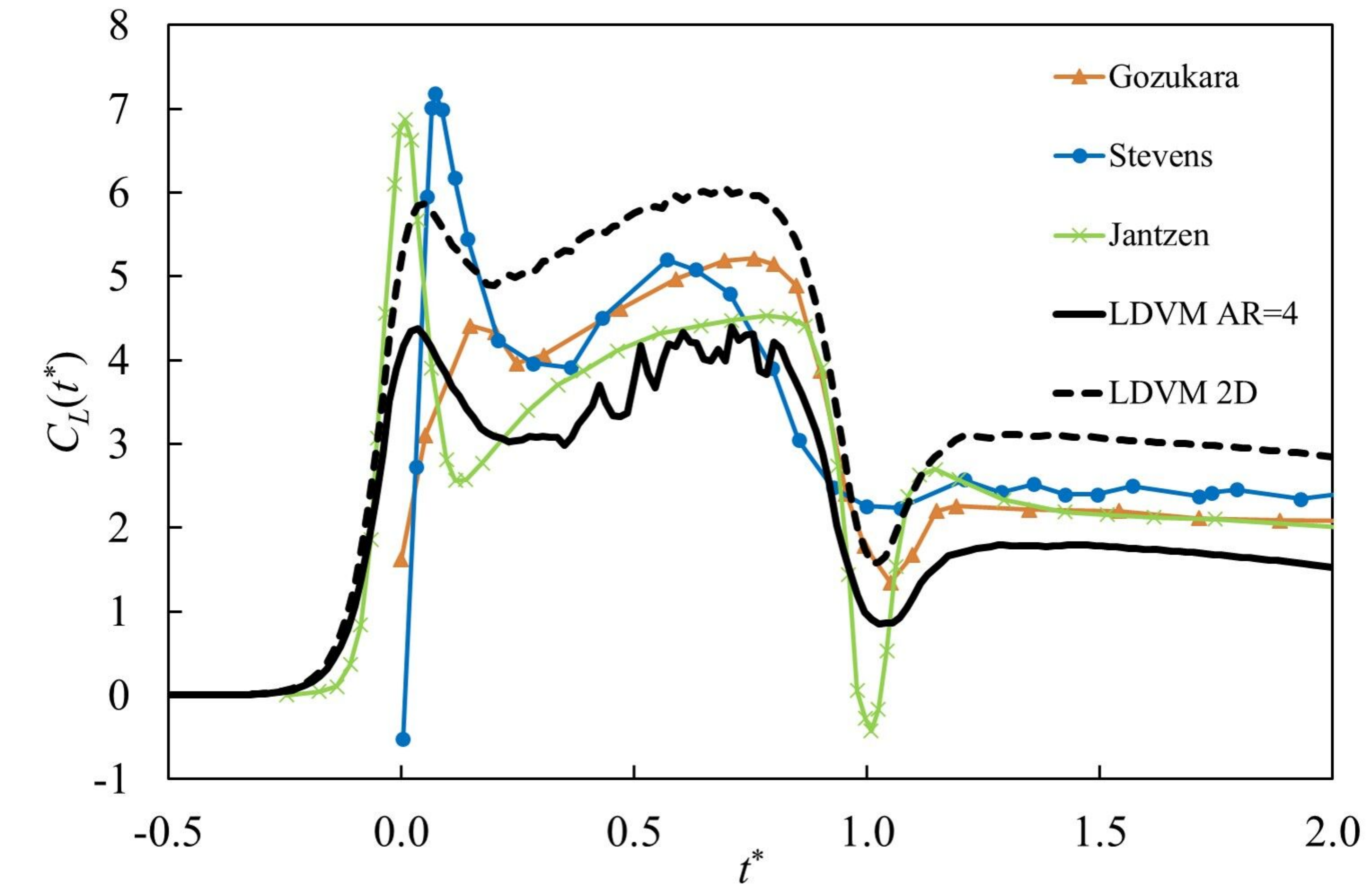

8
7
6
5
4
3
2
1
0
-1
$C_L(t^*)$
-0.5
0.0
0.5
1.0
1.5
2.0
t^*
Gozukara
Stevens
Jantzen
LDVM AR=4
LDVM 2D

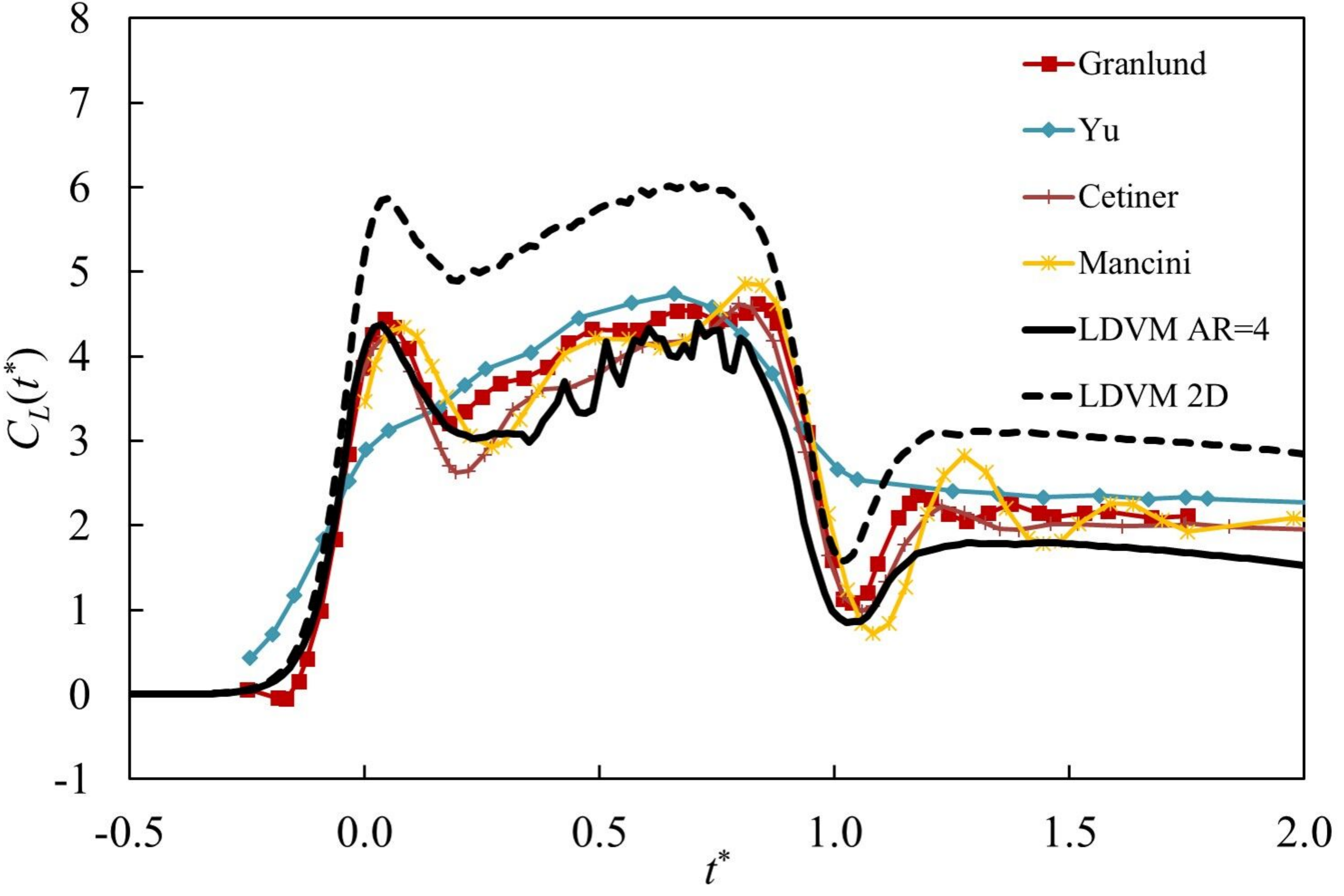

Granlund
Yu
Cetiner
Mancini
LDVM AR=4
LDVM 2D
$C_L(t^*)$
t^*
8
7
6
5
4
3
2
1
0
-1
-0.5
0.0
0.5
1.0
1.5
2.0

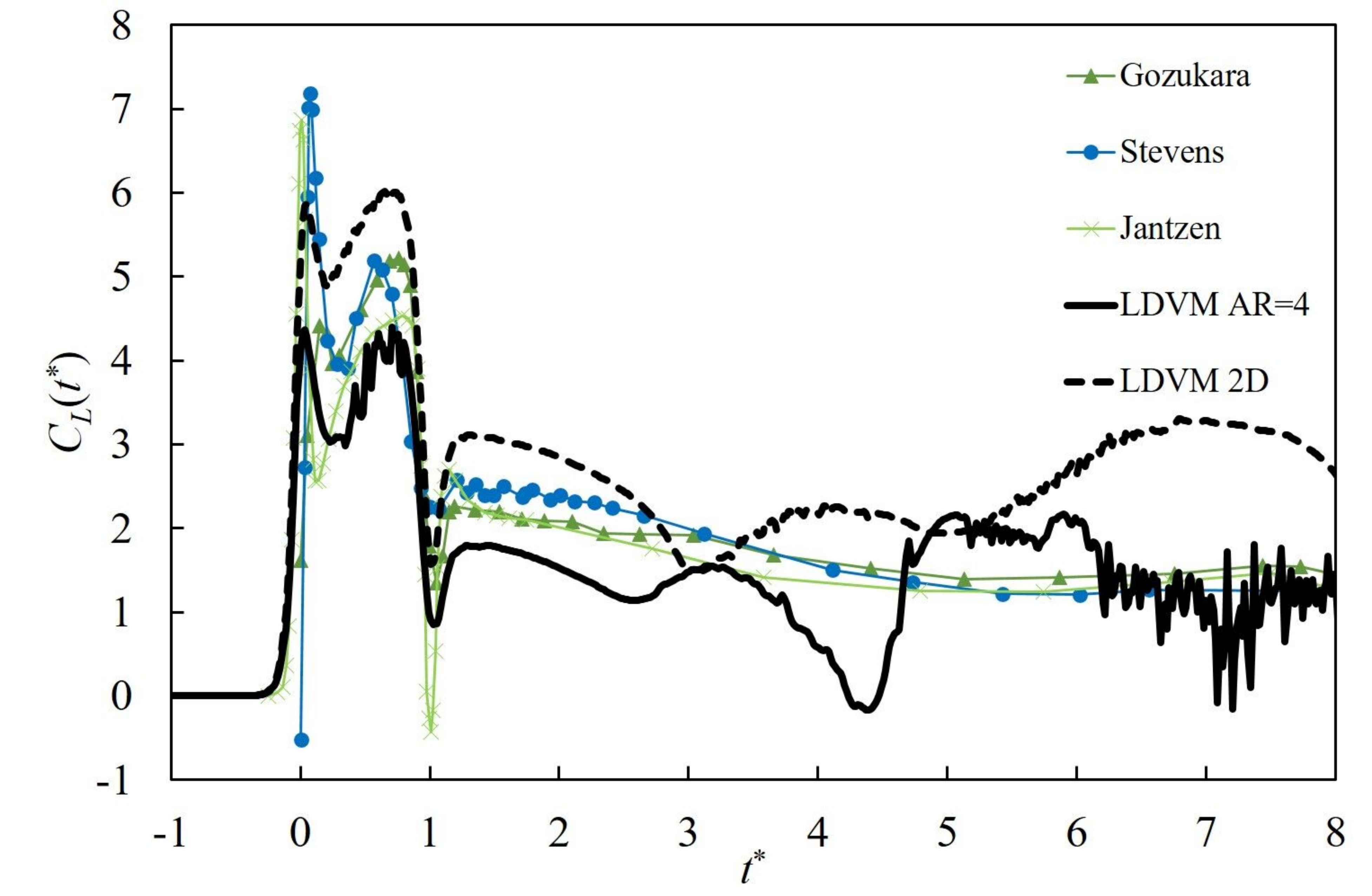

Gozukara
Stevens
Jantzen
LDVM AR=4
LDVM 2D
$C_L(t^*)$
t^*
8
7
6
5
4
3
2
1
0
-1
-1
0
1
2
3
4
5
6
7
8

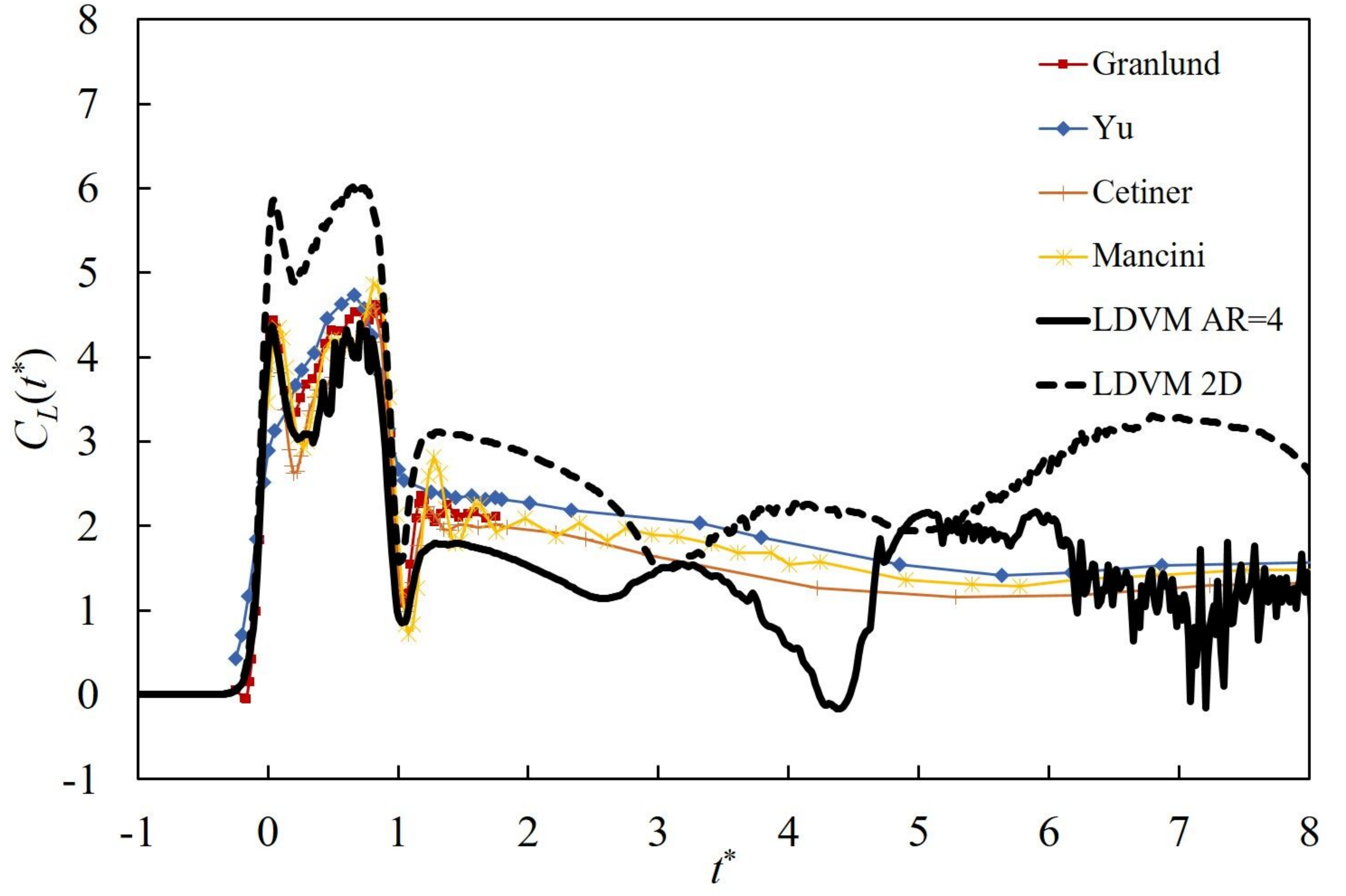

Granlund
Yu
Cetiner
Mancini
LDVM AR=4
LDVM 2D
$C_L(t^*)$
t^*

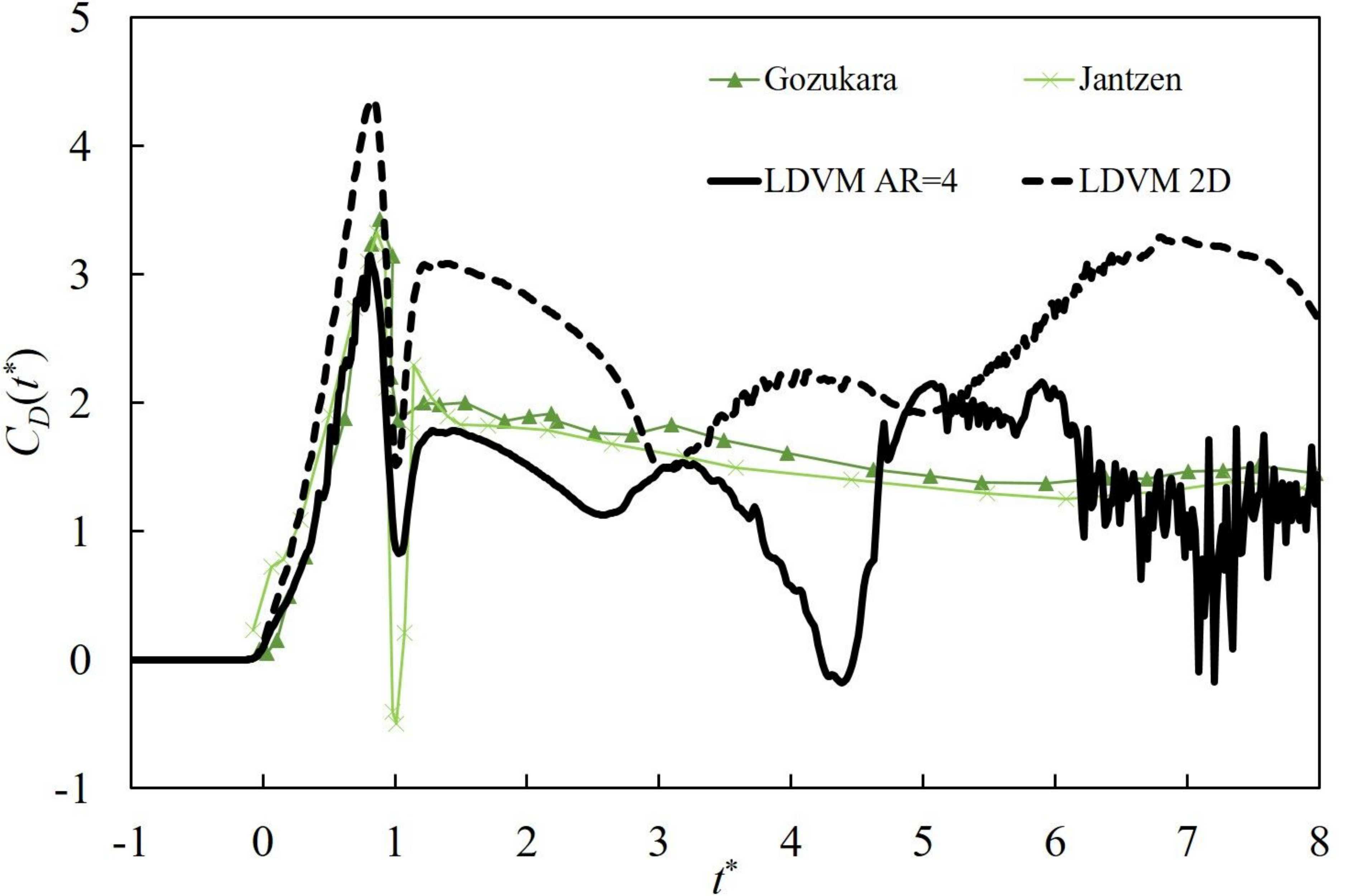

Gozukara
Jantzen
LDVM AR=4
LDVM 2D
$C_D(t^*)$
t^*
5
4
3
2
1
0
-1
-1
0
1
2
3
4
5
6
7
8

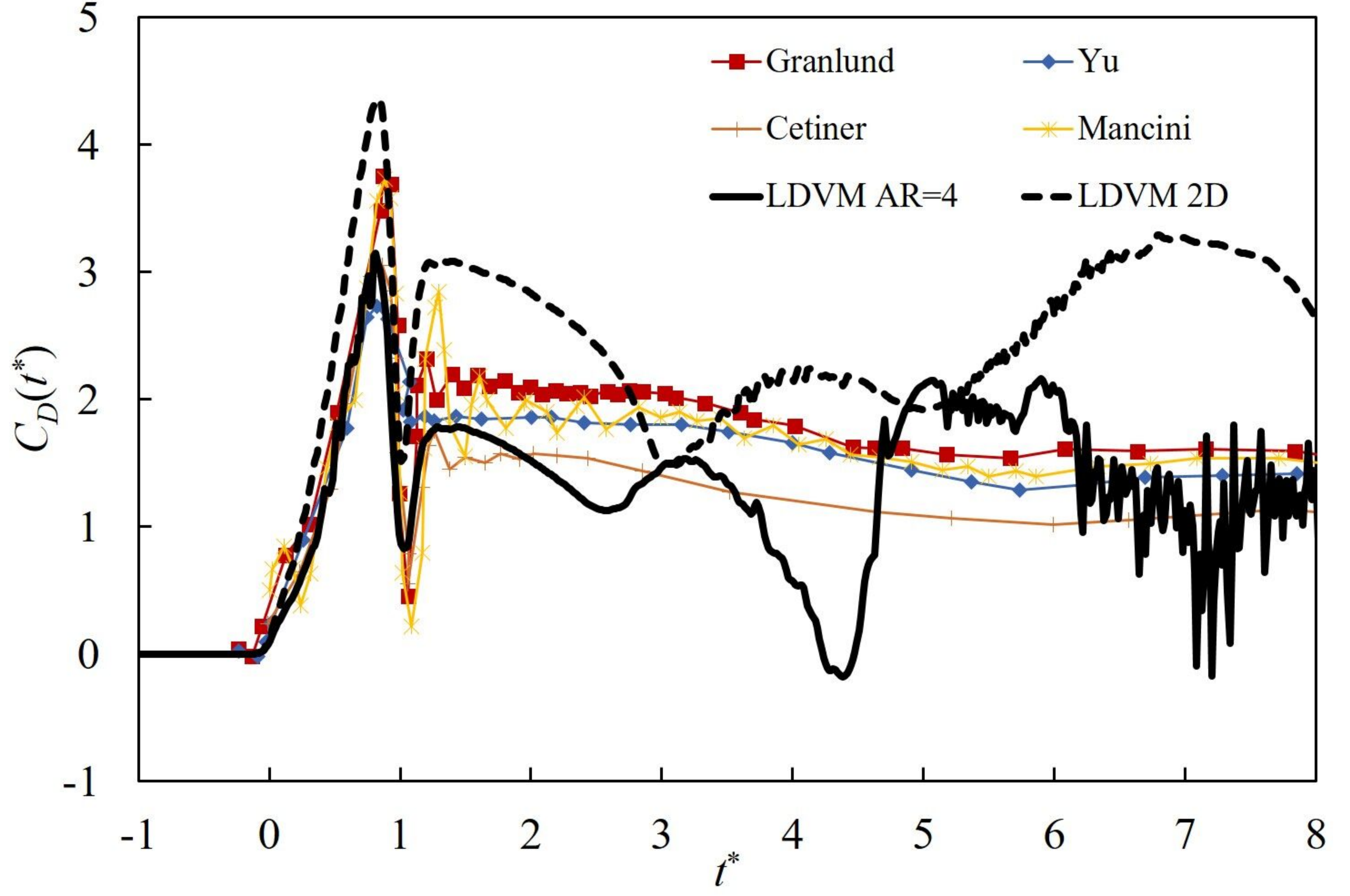

Granlund
Yu
Cetiner
Mancini
LDVM AR=4
LDVM 2D
$C_D(t^*)$
t^*
5
4
3
2
1
0
-1
-1
0
1
2
3
4
5
6
7
8

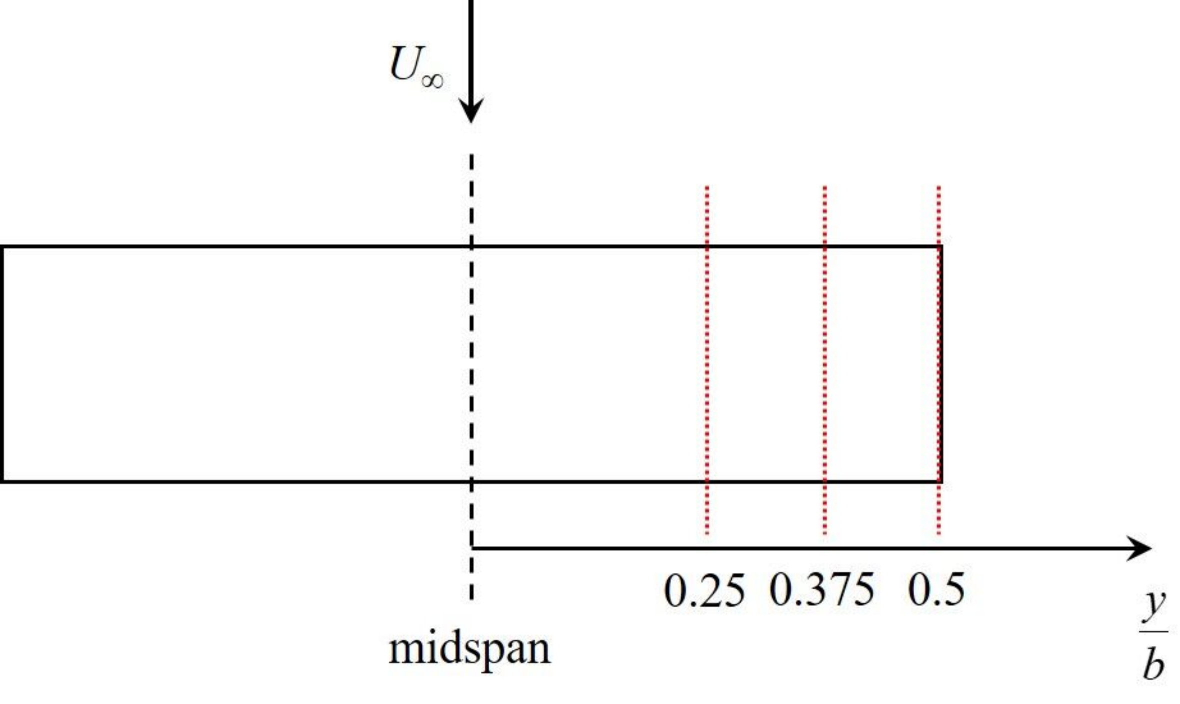

U_∞
0.25
0.375
0.5
$\frac{y}{b}$
midspan

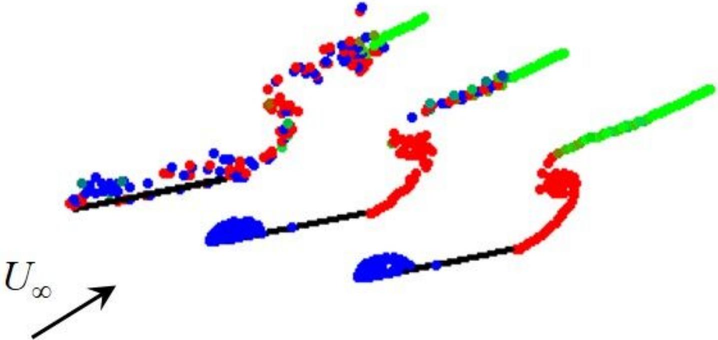
U_∞

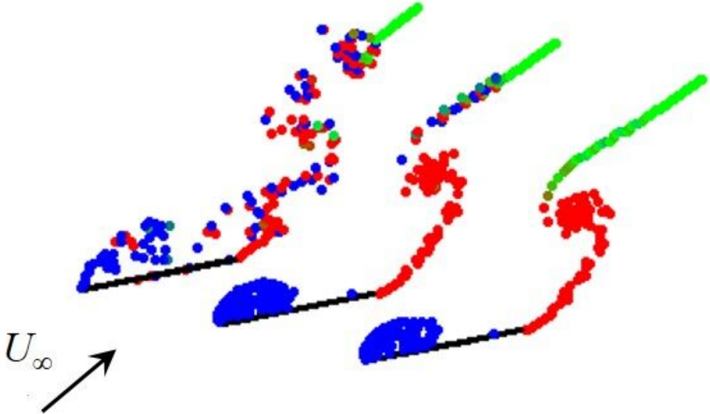
U_∞

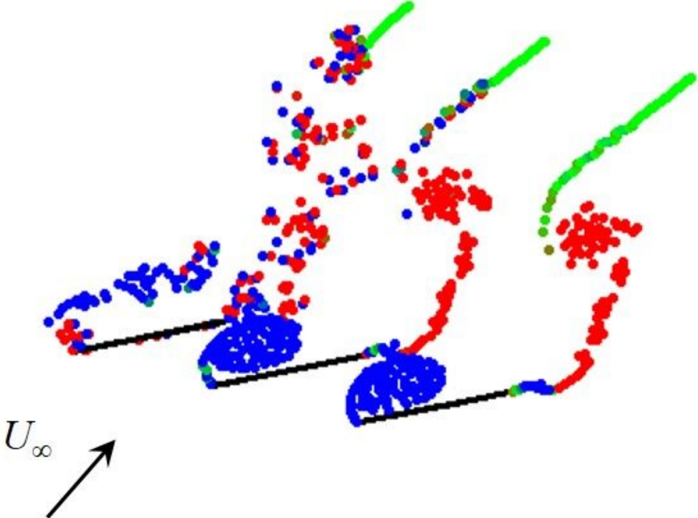
U_∞

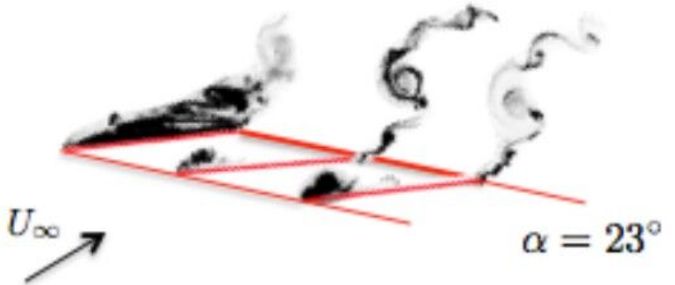

U_∞
$\alpha = 23^\circ$

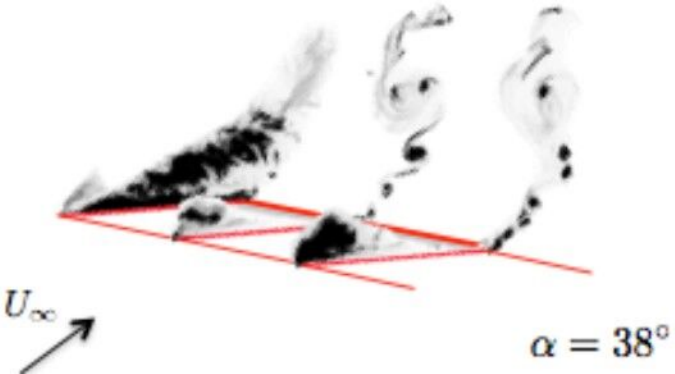

U_∞
$\alpha = 38^\circ$

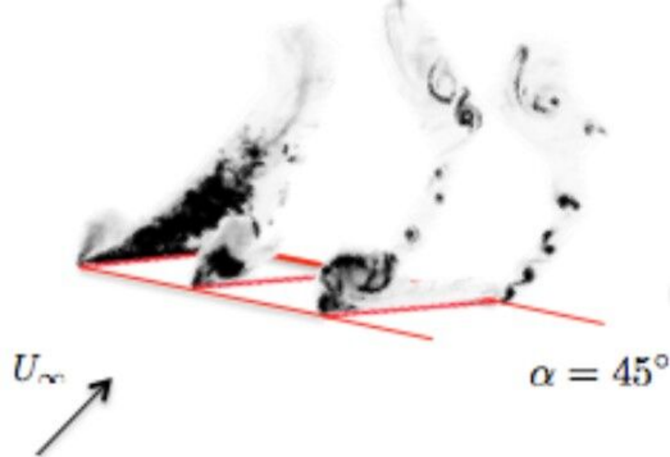

U_∞
$\alpha = 45°$

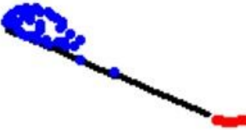

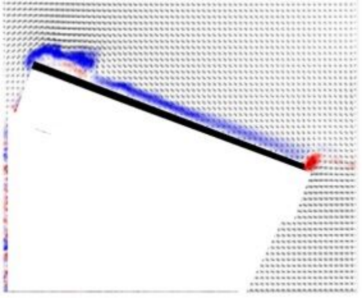

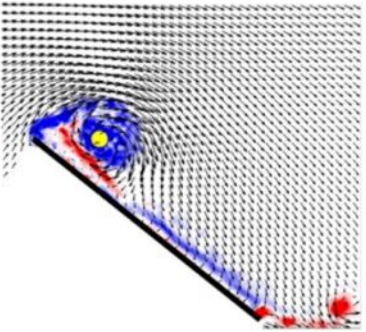

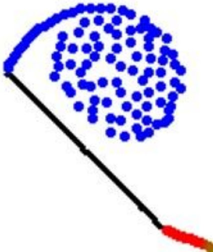

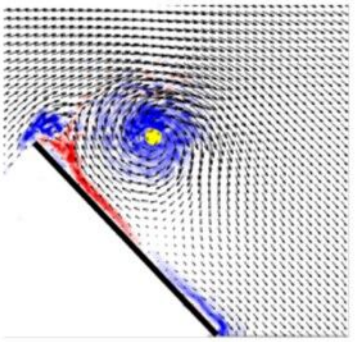

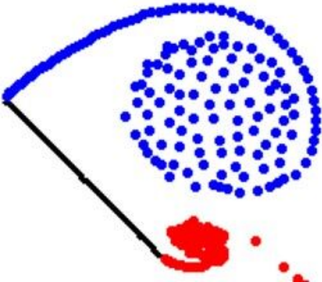

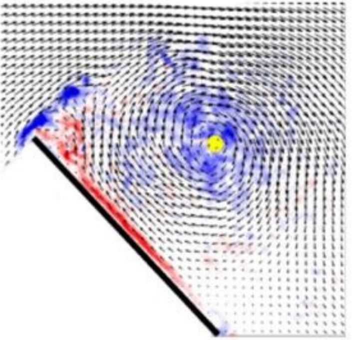

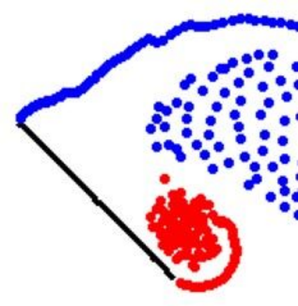

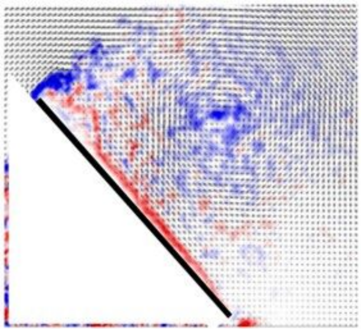

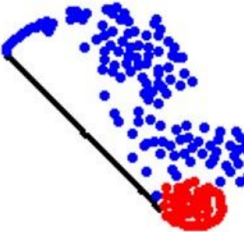

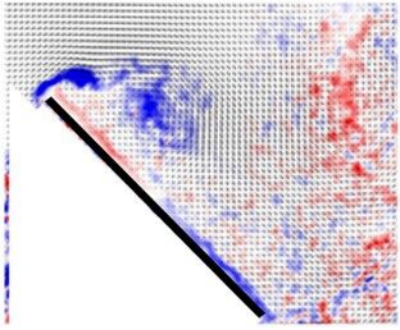

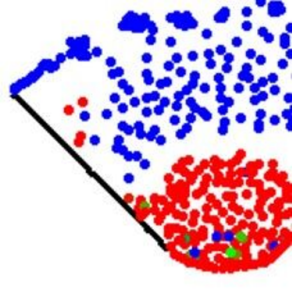

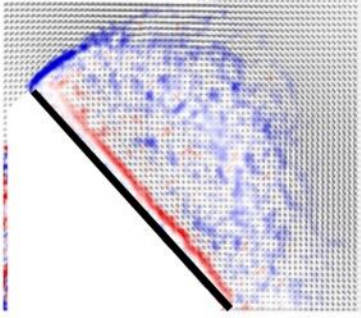

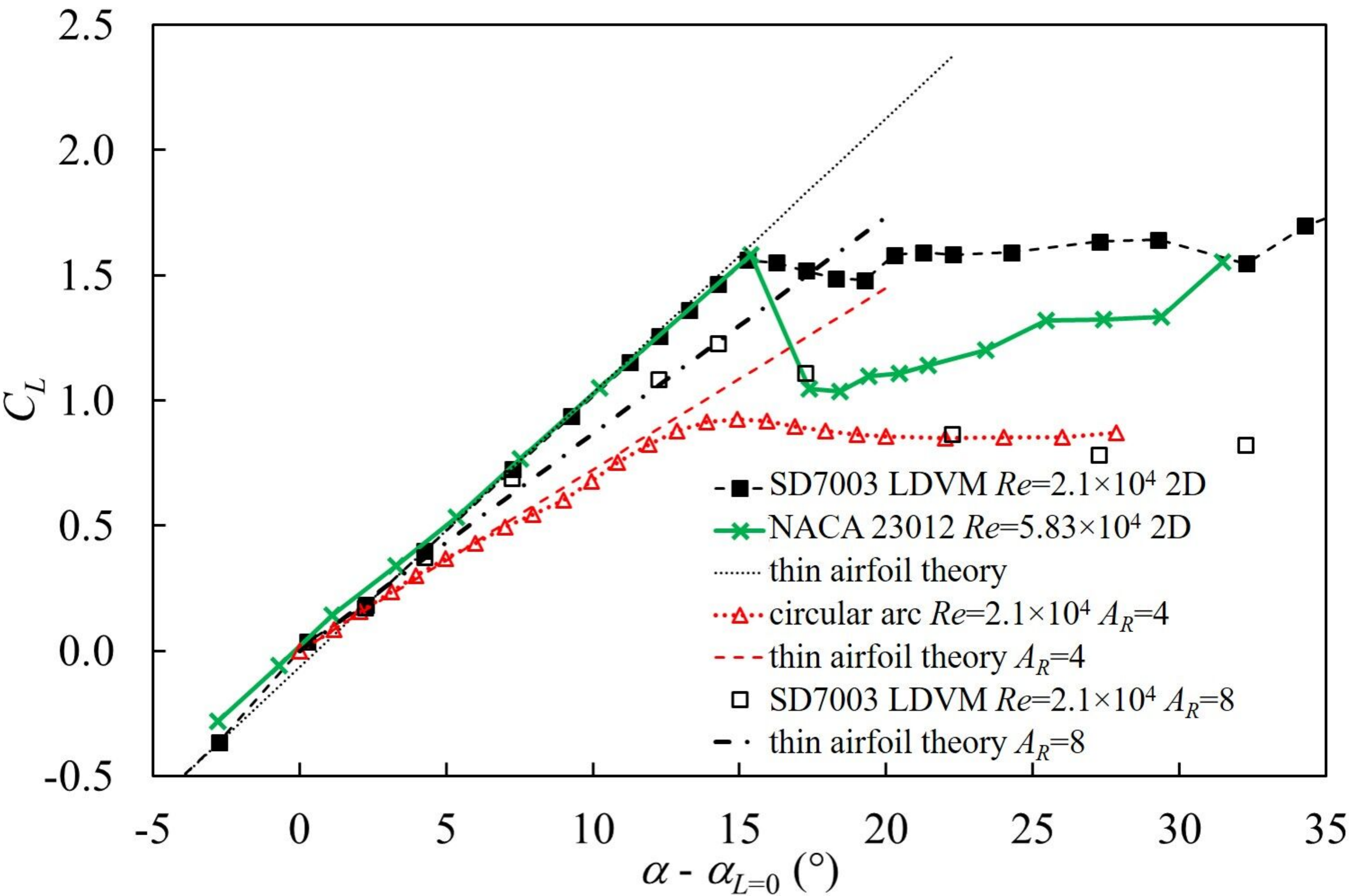

C_L
2.5
2.0
1.5
1.0
0.5
0.0
-0.5
-5
0
5
10
15
20
25
30
35
α - $\alpha_{L=0}$ (°)
SD7003 LDVM Re=2.1×10^4 2D
NACA 23012 Re=5.83×10^4 2D
thin airfoil theory
circular arc Re=2.1×10^4 A_R=4
thin airfoil theory A_R=4
SD7003 LDVM Re=2.1×10^4 A_R=8
thin airfoil theory A_R=8

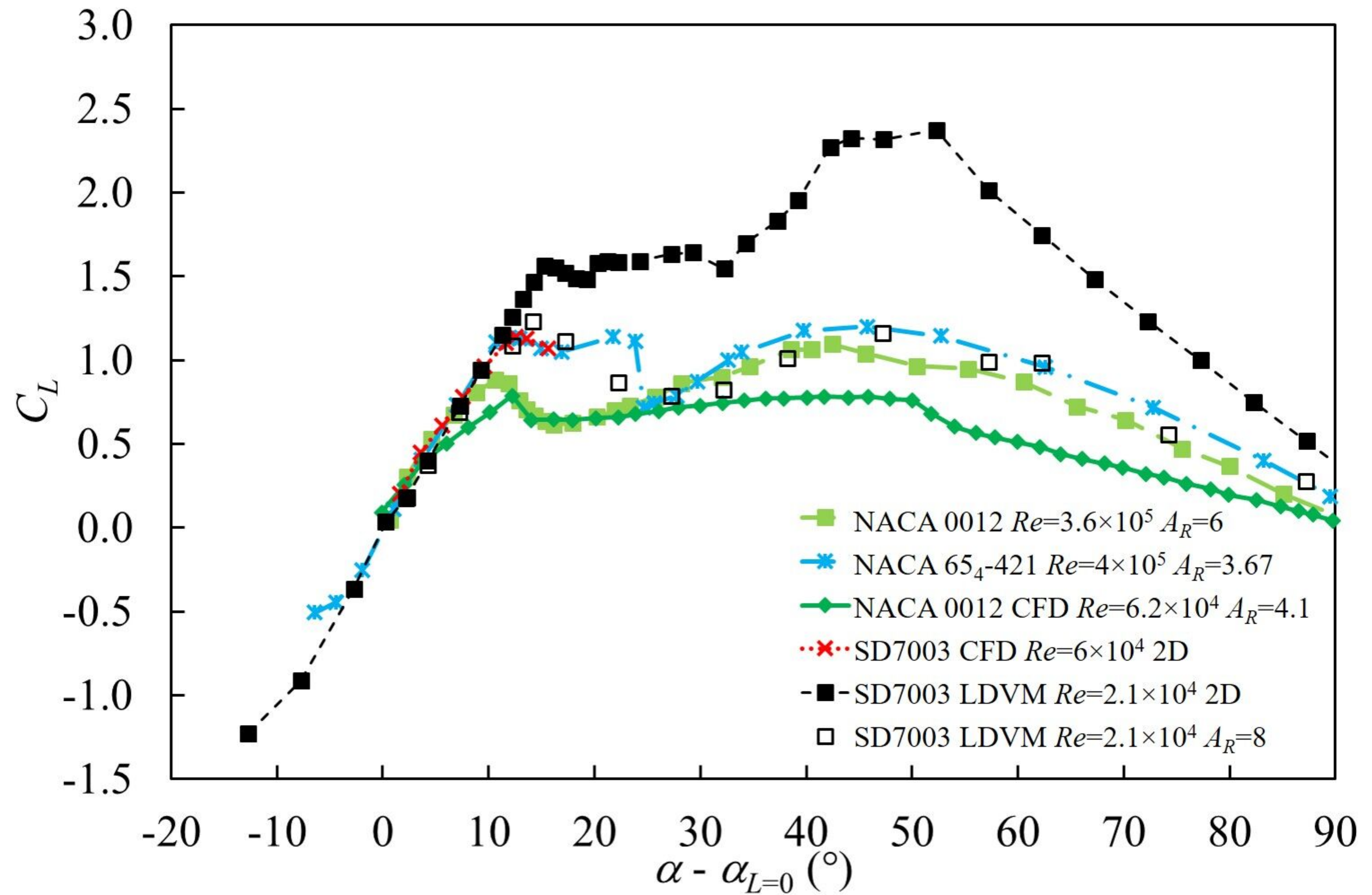
3.0
2.5
2.0
1.5
1.0
0.5
0.0
-0.5
-1.0
-1.5
C_L
-20
-10
0
10
20
30
40
50
60
70
80
90
α - $\alpha_{L=0}$ (°)
NACA 0012 Re=3.6×10^5 A_R=6
NACA 65$_4$-421 Re=4×10^5 A_R=3.67
NACA 0012 CFD Re=6.2×10^4 A_R=4.1
SD7003 CFD Re=6×10^4 2D
SD7003 LDVM Re=2.1×10^4 2D
SD7003 LDVM Re=2.1×10^4 A_R=8

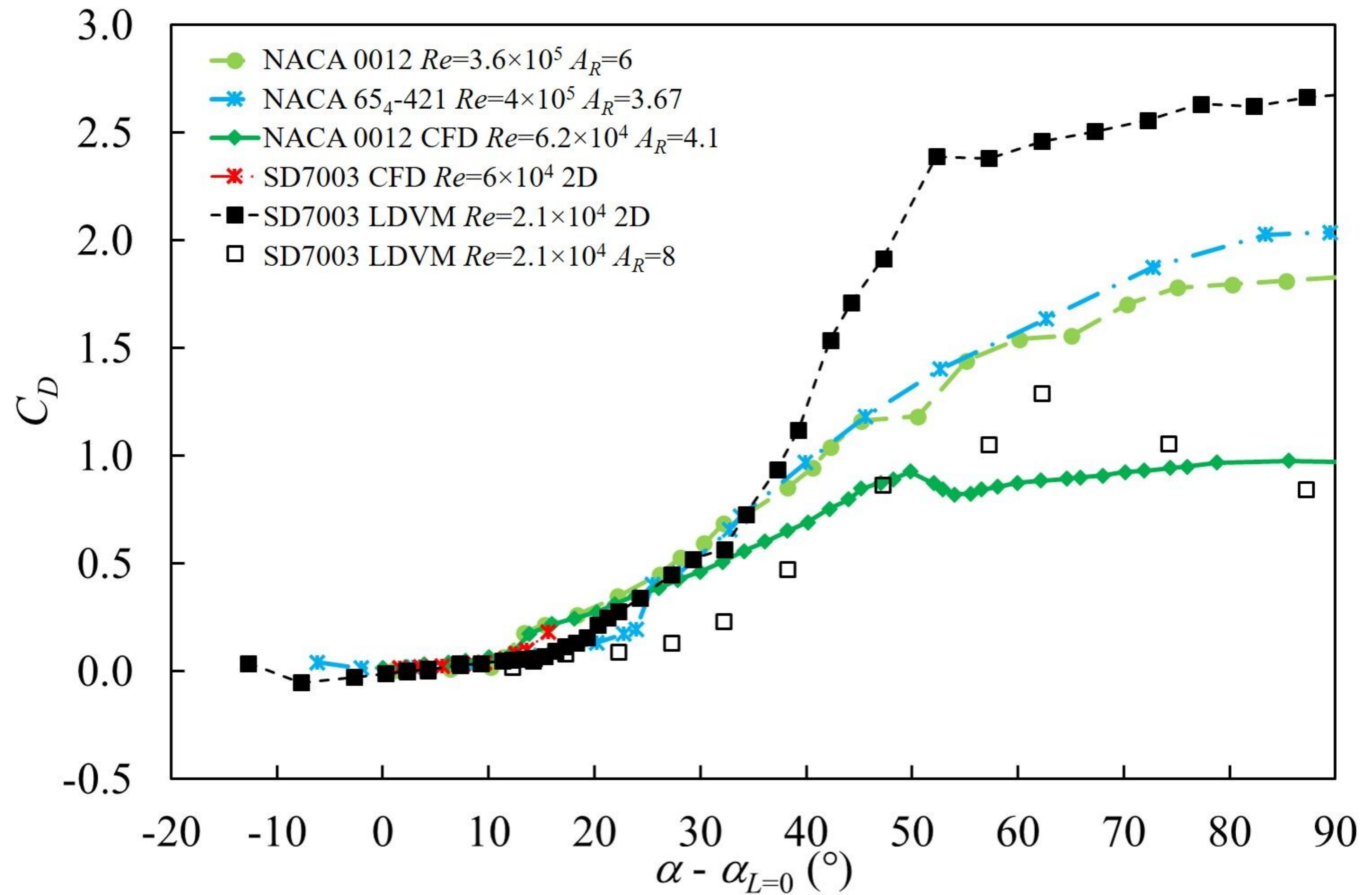
NACA 0012 Re=3.6×10^5 A_R=6
NACA 65_4-421 Re=4×10^5 A_R=3.67
NACA 0012 CFD Re=6.2×10^4 A_R=4.1
SD7003 CFD Re=6×10^4 2D
SD7003 LDVM Re=2.1×10^4 2D
SD7003 LDVM Re=2.1×10^4 A_R=8
C_D
α - α_L=0 (°)
3.0
2.5
2.0
1.5
1.0
0.5
0.0
-0.5
-20
-10
0
10
20
30
40
50
60
70
80
90

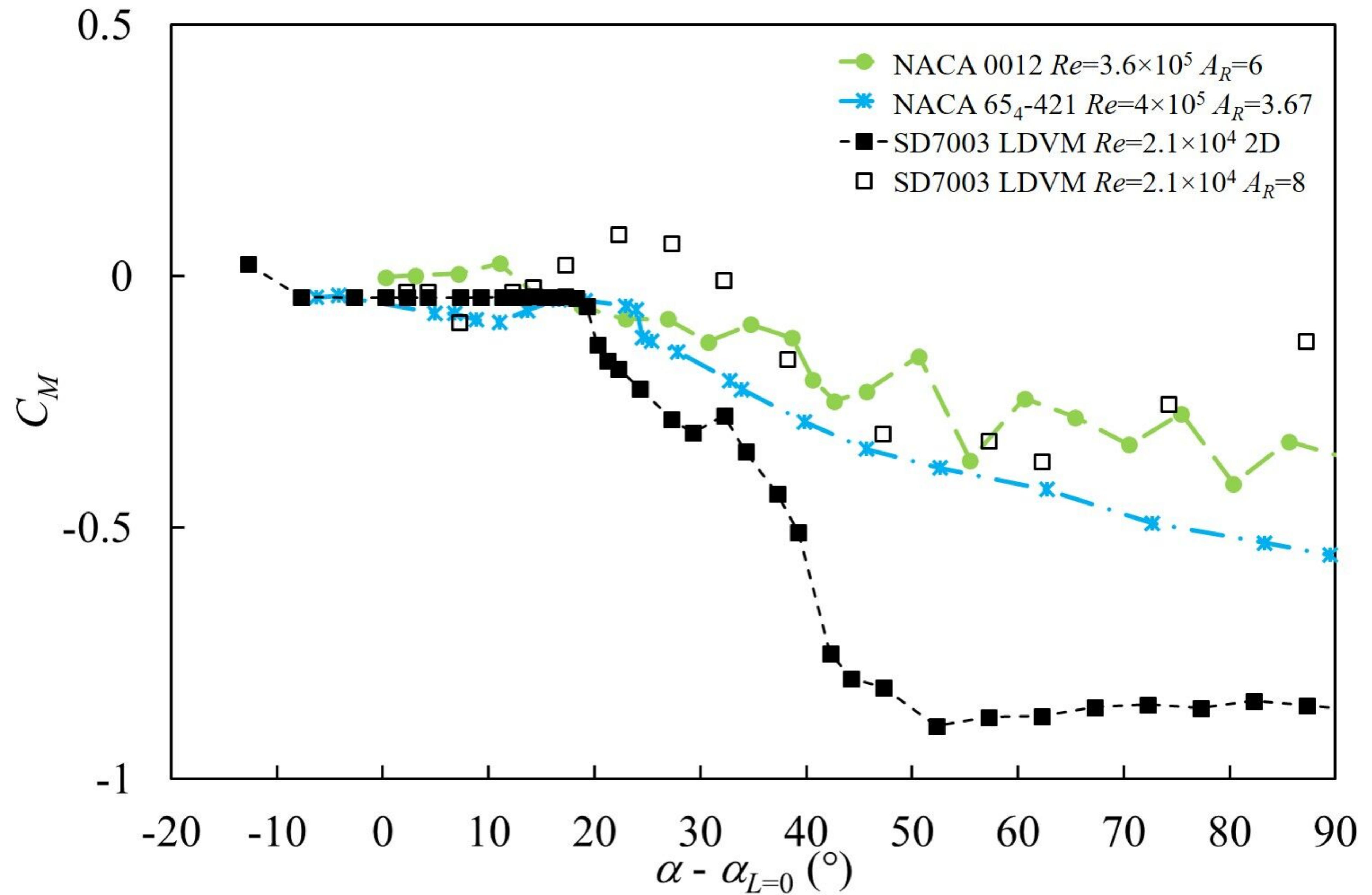

0.5
0
-0.5
-1
C_M
-20
-10
0
10
20
30
40
50
60
70
80
90
α - $\alpha_{L=0}$ (°)
NACA 0012 Re=3.6×10^5 A_R=6
NACA 65$_4$-421 Re=4×10^5 A_R=3.67
SD7003 LDVM Re=2.1×10^4 2D
SD7003 LDVM Re=2.1×10^4 A_R=8